s

Attachment/detachment of cortical myosin regulates cell junction exchange during cell rearrangement

Keisuke Ikawa[1,2,3,*], Shuji Ishihara[4,5], Yoichiro Tamori[6], and Kaoru Sugimura[1,2,5,7,*,#]

1: Department of Biological Sciences, Graduate School of Science, The University of Tokyo, Tokyo, Japan
2: Institute for Integrated Cell-Material Sciences (WPI-iCeMS), Kyoto University, Kyoto, Japan
3: Division of Biological Science, Graduate School of Science, Nagoya University, Aichi, Japan
4: Department of Integrated Sciences, Graduate School of Arts and Sciences, The University of Tokyo, Tokyo, Japan
5: Universal Biology Institute, The University of Tokyo, Tokyo, Japan
6: Department of Molecular Oncology, Graduate School of Medicine, Kyoto University, Kyoto, Japan
7: Department of Computational Biology and Medical Sciences, Graduate School of Frontier Sciences, The University of Tokyo, Chiba, Japan

* Corresponding authors:
sugimura@bs.s.u-tokyo.ac.jp (KS), ikawa.keisuke.w6@f.mail.nagoya-u.ac.jp (KI)

[#] The lead contact

Abstract

Epithelial cells remodel cell adhesion and change their neighbors to shape a tissue. This cell rearrangement proceeds in three steps: the shrinkage of a junction, exchange of junctions, and elongation of the newly generated junction. Herein, by combining live imaging and physical modeling, we showed that the formation of myosin-II (myo-II) cables around the cell vertices underlies the exchange of junctions. The local and transient detachment of myo-II from the cell cortex is coupled with the junction shrinkage and elongation via an interplay between the LIM domain-containing protein Jub and the tricellular junction protein M6. Furthermore, we developed a mechanical model based on the wetting theory and clarified the way by which the physical properties of myo-II cables are integrated with the junction geometry to induce the transition between the attached and detached states and support the unidirectionality of cell rearrangement. Collectively, the present study elucidates the orchestration of geometry, mechanics and signaling for exchanging junctions.

Introduction

Cell rearrangement plays a fundamental role in shaping a tissue and developing multicellular patterns[1–5]. Cell rearrangement proceeds in three steps: the shrinkage of a junction, exchange of junctions around the cell vertex (four-way or higher-folded), and elongation of the newly generated junction. The molecular mechanisms underlying junction shrinkage and elongation have been well characterized. At the apical level, medial actomyosin flow and junctional recruitment of myosin-II (myo-II) lead to the generation of forces that shrink and elongate a junction[2–6]. At the basolateral level, actin-rich protrusions deform the cell membrane[7]. In sharp contrast, little is known regarding how epithelial cells exchange junctions during cell rearrangement.

Molecules comprising the junctional structure play essential roles in the development of epithelial tissue, where the bicellular junction (bCJ) including the adherence junction (AJ) adheres cells, and the tricellular junction (TCJ) seals the tissue at the cell vertex[2,8,9]. During cell rearrangement, as the bCJ dynamically changes its length, the position of the TCJ changes. The junction deformation and vertex displacement are determined by the balance between the constriction force generated by myo-II and the adhesive force generated by cell adhesion molecules such as E-cadherin[2–6]. The mechanical force balance is tuned by actin-AJ linkers, which are responsible for the linkage between actomyosin and E-cadherin, and TCJ proteins, which are a class of proteins comprising the cell vertex structures, to maintain cell adhesion during the junction shrinkage and control the speed of junction elongation[10–15]. The localization and activity of these molecules need to be coordinated such that cell adhesion is weakened specifically at short junctions around the cell vertex and such that *de novo* formation of cell adhesion is initiated between the correct pair of cells. The mechanism underlying the coordination of cell adhesion and the regulatory molecules during the junction exchange is unclear.

Recent studies from others and us identified a cytoskeleton structure that could be critical in the junction exchange[10,12,16]. We showed that myo-II transiently forms rectangle-shaped cables around the cell vertices at the AJ plane in *Drosophila* wing epithelium (Fig. 1a, b; hereafter called rsMC (rectangle-shaped myo-II cables))[16]. Such local detachment of myo-II from short junctions has been reported in other epithelial tissues[10,12]. The rsMC may represent a temporally loosened junctional structure, which facilitates the reconnection of junctions. However, the molecular and physical basis of rsMC dynamics and function have not been studied extensively.

Here, we sought to identify the mechanism by which apical junctions are exchanged during cell rearrangement in the *Drosophila* wing epithelium. The findings demonstrate that the precise control of rsMC formation supports the exchange of junctions and the stabilization of newly generated junctions. The rsMC formation is coupled with the junction shrinkage and elongation via an interplay between the LIM domain-containing protein Jub and the tricellular junction protein M6. A mechanical

model based on the wetting theory can explain the junction-length-dependent transition between the detached and attached states of cortical myo-II and the unidirectionality of cell rearrangement. The coupling between junction geometry, mechanics, and signaling identified in the present study may function in other aspects of morphogenesis, as all morphogenetic events are associated with spatio-temporal changes in these three aspects.

Results

Local and transient formation of rectangle-shaped myo-II cables during the junction exchange

To address the mechanism by which epithelial cells exchange junctions, we analyzed the distribution of molecules during cell rearrangement in the *Drosophila* wing epithelium (see Supplementary Fig. 1a, b for schematics of the wing). Following the shrinkage of anterior-posterior (AP) junction, myo-II detached from the junction (Fig. 1b, blue arrowheads in Fig. 1c, Supplementary Video 1). We designated the subcellular structure as the rsMC (rectangle-shaped myo-II cables). DE-cadherin (DE-cad) became more diffusively distributed around the junctions (green arrowhead in Fig. 1c), and the plasma membrane marker mCD8-GFP was localized inside the rsMC (blue arrowhead in Fig. 1f). These data indicate that a junction structure was present inside the rsMC. As shown in Fig. 1g–k, a rsMC was formed at the AJ labelled by DE-cad, apical to the septate junction (SJ) labeled by Discs large (Dlg).

rsMC was a transient structure with an average duration time of 4.3 ± 4.1 min (n = 69). The myo-II signal intensity was, on average, higher along the vertical (AP) edges of the rsMC (Fig. 1d; we excluded medial pools of actomyosin from our analysis because they are not densely accumulated in the pupal wing). The separation of two bright spots of myo-II (yellow arrowheads in Fig. 1c) proceeded concomitantly with the decrease in the myo-II signal intensity on the horizontal edges of rsMC (Fig. 1e). Eventually, myo-II became more uniformly distributed along the newly formed proximal-distal (PD) junction, indicating the reattachment of myo-II cables to the junction (magenta arrowheads in Fig. 1c).

As cortical myosin cables dynamically change their shape during junction exchange, reorganization of other cellular structures occurs. We found that bright dots of Sidekick (Sdk)[10–12], a tricellular AJ (tAJ) protein, apposed inside the rsMC, were then separated along the horizontal direction as a new junction was formed (Fig. 1l). This observation suggests that the disassembly and reassembly of TCJs occur at the AJ level during junction exchange. To probe actin cytoskeleton, we clonally expressed a F-actin marker, Life-Act-GFP. Prior to the separation of myo-II cables, actin protrusions invaded the rsMC at the AJ, whereas no significant actin-rich protrusions were detected at the basolateral side of the cells (Supplementary Fig. 1k, l, Supplementary Video 2). Collectively, these data showed that in the wing, the junction exchange is accompanied by the formation of the orderly structure comprising myo-II, the actin cytoskeleton and junction components at the AJ.

rsMC formation is regulated by actin-AJ linkers including Jub

Next, we searched for molecules underlying rsMC dynamics. We identified actin-AJ linkers that strengthen the linkage between actomyosin and AJ, including the LIM domain-containing protein Jub/Ajuba and PDZ protein Canoe (Cno)/Afadin[14,15,17–21],

136 as important regulators of the process. Our time-lapse analysis detected pleiotropic
137 phenotypes in *jub* RNAi cells: (i) the precocious formation of rsMCs from longer
138 junctions, which resulted in the enlargement of the rsMC, (ii) prolonged duration of the
139 rsMC, and (iii) failure in the reattachment of myo-II to the newly formed PD junction,
140 which resulted in the destabilization of new junction and subsequent reverse
141 reconnection of junctions (Fig. 2a, c–e, Supplementary Fig. 2a, b, Supplementary Fig.
142 3b, Supplementary Video 3). *jub* RNAi cells retained a plasma membrane marker
143 mCD8-GFP[22] in the enlarged rsMC (Fig. 2f), suggesting that *jub* RNAi phenotypes
144 were not due to the defect of the plasma membrane. *cno* RNAi and *Dα-catenin* (*Dα-*
145 *cat*) RNAi, but not *vinculin* (*vinc*) RNAi, altered the rsMC dynamics and resulted in
146 the failure in junction exchange, similar to *jub* RNAi (Fig. 2b–e, Supplementary Fig.
147 2c–e, Supplementary Fig. 3b, Supplementary Video 3). The signal intensity of myo-II
148 and DE-cad hardly changed on *vinc* RNAi, whereas *jub* RNAi decreased the DE-cad
149 level and *cno* and *Dα-cat* RNAi increased the myo-II level (Fig. 2h, Supplementary
150 Fig. 3a). The absence of rsMC malformation in *vinc* RNAi cells was consistent with
151 the hierarchy in co-dependence of actin-AJ linkers in their subcellular distribution
152 (Supplementary Fig. 4 and its legends). The correlation coefficient between the rsMC
153 area and average area of cells surrounding the rsMC was 0.04 (Fig. 2g and
154 Supplementary Fig. 1j), which strongly suggests that the enlargement of rsMC was not
155 the secondary consequence of the change in cell size.
156 To further explore the involvement of Jub, Cno, and Dα-cat in rsMC dynamics,
157 we analyzed their distributions in *wild-type* (*WT*) cells. We found that the Jub signal
158 was weakened specifically at the shrinking and reconnecting junctions (Fig. 2i, j,
159 Supplementary Video 4). The Cno and Dα-cat signals decreased to a lesser extent
160 during the junction exchange (Supplementary Fig. 3h–k). These findings suggested that
161 Jub, Cno, and Dα-cat prevented the detachment of cortical myo-II during the early
162 phase of cell rearrangement, and that tuning the level of junctional Jub is important for
163 the correct formation of the rsMC and subsequent completion of junction reconnection.
164
165 **M6 is responsible for the reduced level of Jub during junction exchange**
166 Next, we investigated the mechanism responsible for the reduction of Jub levels during
167 the junction exchange. We have shown that actin interacting protein 1 (AIP1) and
168 cofilin retained Jub, Cno and Dα-cat at the shrinking AP junctions to prevent the
169 precocious formation of the rsMC (Supplementary Fig. 5a, b; *flare* (*flr*) and *twinstar*
170 (*tsr*) encode *Drosophila aip1* gene and *cofilin* gene, respectively) (ref. 16 and this
171 study). Thus, AIP1 and cofilin may be eliminated from the AJ immediately before
172 junction exchange, leading to the reduction of Jub levels. However, both AIP1 and
173 cofilin were present along the reconnecting junctions; a strong AIP1 signal was detected
174 inside the rsMC, and the cofilin signal was maintained after the junction shrinkage
175 (Supplementary Fig. 5c–e). These data indicated that the rsMC formation is not
176 accounted for by the decrease in AIP1 and/or cofilin levels at short junctions.

177 Alternatively, we noticed that a rsMC-like structure was occasionally formed
178 around the vertex of the non-remodeling junctions (Fig. 3a). This observation led us to
179 a hypothesis that TCJ proteins[8,9] reduce junctional Jub levels to promote the rsMC
180 formation. To test this hypothesis, we performed loss-of-function experiments on TCJ
181 proteins. We found that RNAi of *m6*, which encodes a component of the tricellular SJ
182 (tSJ)[23–25], increased the fraction of long-lasting rsMCs, without inducing the drastic
183 malformation of the rsMC (Fig. 3b–e, Supplementary Fig. 2h–j, Supplementary Video
184 5). Jub was persistently retained inside such long-lasting rsMCs (Fig. 3f, g,
185 Supplementary Video 6). Taken together, our data strongly suggest that the TCJ protein,
186 M6, weakens the linkage between myosin and AJ by reducing the Jub level.
187 It has been reported that M6 and the tSJ protein Anakonda (Aka) localize to
188 the TCJ in a mutually dependent manner and that they cooperate in the TJC assembly
189 in other epithelial tissues[24,26]. Thus, it is possible that Aka works with M6 in the
190 junction exchange in the wing. However, we detected no strong phenotype of the rsMC
191 in *aka* RNAi cells (Fig. 3c–e, Supplementary Fig. 2f, Supplementary Fig. 5l). The
192 signal intensity of M6 was decreased upon *aka* RNAi, but M6 still localized at the cell
193 periphery including vertices (Fig. 3h, i). On the contrary, the Aka signal was hardly
194 detected in *m6* RNAi cells (Fig. 3j, k). The localization of Aka was more severely
195 affected by *m6* RNAi, which might lead to the difference in the defect in the rsMC
196 dynamics under the condition employed in this study.
197 RNAi of *sdk*, which encodes the tAJ protein Sdk[10–12], did not strongly interfere
198 with the rsMC dynamics (Fig. 3c–e, Supplementary Fig. 5m). We confirmed that the
199 signal of Sdk-YFP dropped below the detection limit upon *sdk* RNAi (Supplementary
200 Fig. 2g). The elongation of newly generated junctions was slowed down upon *sdk* RNAi
201 in the wing (WT: 0.23 ± 0.20 μm/min, *sdk* RNAi: 0.09 ± 0.04 μm/min). This agrees
202 with previous reports on male genitalia[10]. These results suggest that *sdk* RNAi is
203 effective and that M6 and Sdk are responsible for different aspects of cell
204 rearrangement.
205
206 **Interplay between M6 and Jub during junction exchange**
207 Having established that M6 reduces the junctional Jub level during the junctional
208 exchange, we investigated whether there is a counter-regulation from Jub to M6. M6
209 predominantly localized at the tSJ in *WT* (Fig. 3l–n). In *jub* RNAi cells, however, M6
210 was also detected at the AJ, indicating that M6 could stay at the AJ from which Jub was
211 eliminated (Fig. 3o–q). M6 appeared at the AJ inside the enlarged rsMC of *flr* or *tsr*
212 RNAi cells (Supplementary Fig. 5f–k), which is consistent with the loss of Jub along
213 the remodeling junctions in these cells (Supplementary Fig. 5a, b). Collectively, our
214 data uncovered an interplay between Jub and M6 during cell rearrangement.
215 Based on these findings, we propose that the junction shrinkage and elongation
216 autonomously adjust the interplay between Jub and M6 to reconnect junctions. During
217 the early phase of cell rearrangement, M6, which localizes at the vertex of the long

remodeling junction, cannot exert a strong inhibitory effect on junctional Jub. Thus, Jub can maintain the linkage between cortical myo-II and the AJ. As cell rearrangement proceeds, the junction shrinkage brings the vertices at both ends of remodeling junction into proximity, which can elevate the inhibitory effect of M6 on Jub. Once the level of Jub starts to decrease, M6 gains more access to the AJ. This positive feedback leads to the detachment of cortical myo-II, specifically at short junctions. Subsequently, the elongation of the newly formed junction activates the feedback in the opposite direction, which allows the reattachment of cortical myo-II to junctions for the completion of junction reconnection.

Junction geometry and mechanics govern the detachment of cortical myo-II cables for junction exchange

To understand the physical basis of junction exchange, we constructed a simple mechanical model based on the wetting theory[27] and explored how changes in mechanical parameters, which are regulated by the molecular interactions described above, control the attachment and detachment of cortical myo-II cables to the junction. First, we considered the attached and detached states of cortical myo-II cables in a single cell (blue lines and red lines, respectively, in Fig. 4a). The myo-II cables are under tension and attached to the junction via the actin-AJ cross linkers. The free energy is originated from the cable's tension and adhesion to the junction, whose energies per unit length are γ and $-\sigma$, respectively, and are uniform in the vicinity of the remodeling junction. Then, the energy cost of tension γ and energy gain of adhesion σ lead to the difference in the free energies of the attached and detached states: $F_d - F_a = -2l(1-\cos\theta)\gamma + \sigma(L_0 + 2l)$ (see Fig. 4a, c–e for definitions and quantifications of geometrical quantities L_0, l, and θ). The detached state is energetically preferable when F_d is smaller than F_a, which results in the rsMC formation.

The analysis of the model indicated that an energy barrier $\Delta F = \sigma L_0$ is present between the attached and detached states (Fig. 4g) and that the detached state is energetically preferable in the region $\gamma > \sigma(L_0 + 2l)/2(1-\cos\theta)l$ with a threshold tension $\gamma^* \equiv \sigma/(1-\cos\theta)$ (Fig. 4h). Thus, large γ and/or small σ favor the detachment of myo-II cables from the junction. In addition, the conditions for the detachment depend on the geometrical quantities as well. For instance, the parameter region of the detached state is enlarged as L_0 decreases (Fig. 4h). The half-angle between connecting junctions θ also controls the threshold tension γ^*; $\gamma^* = \sigma$ when $\theta = 90°$ and γ^* becomes infinitely large as θ reaches to zero. Taken together, the balance between tension γ and adhesion σ, in cooperation with the cell geometry, determines the attachment and detachment of myo-II cables.

The results of the model analysis provided an interpretation of the experimental data. First, the model prediction that the junction shrinkage (*i.e.*, small L_0) lowers the energy barrier and tension required for the detachment is consistent with

the experimental observation that the detachment of myo-II cables is triggered specifically at short remodeling junctions. Second, the half-angle is maintained at approximately $\theta \approx 60°$ during junction shrinkage (the first and second rows of Fig. 4e), suggesting that the change in junction angle is not a main trigger of myo-II detachment in wing cells. Third, as cell rearrangement proceeded, myo-II, which can be regarded as a proxy for active stress[28] contributing to cable tension γ, was enriched (Fig. 4f)[29] and Jub, which contributed to the adhesion energy σ, was eliminated (Fig. 2j). Together, the balance between γ and σ shifted to favor the detached state. Fourth, the model predicts that when σ is uniformly lowered at the junctions, cells can overcome the energy barrier $\Delta F = \sigma L_0$ at large L_0, which is consistent with the loss-of-function phenotypes of actin-AJ linkers (Fig. 2a–e).

Next, we considered myo-II cables in four cells surrounding reconnecting vertices (Fig. 4b). We assumed that detached myo-II cables maintain a rectangular shape. The tension at the vertical (AP) and horizontal (PD) edges of the rectangular rsMC is set as γ and γ', respectively. A similar calculation as described above leads to the condition required for the myo-II detachment as $\gamma(1-\cos\theta)+\gamma'(1-\sin\theta) > \sigma(2+L_0/2l)$ for the detached state (I) in Fig. 4b (Methods). As discussed above, the transition to the detached state is induced by the decrease in L_0 by the junction shrinkage and/or the increase in γ/σ (Fig. 4i). After the junctions are reconnected and the newly generated junction elongates, the condition of the myo-II detachment changes as $\gamma(1-\cos\theta')+\gamma'(1-\sin\theta') > \sigma(2+L_0'/2l)$ (the detached state (II) in Fig. 4b). According to this condition, the decrease in γ or γ' makes the attached state energetically favorable when the tension of the other type of edges of rsMC remains unchanged (Fig. 4j). Consistent with this model prediction, myo-II gradually decreased at the horizontal (PD) edges of myo-II cables, which eventually attached to the newly generated PD junction in *WT* cells (Fig. 1e).

Finally, we quantitatively compared our mechanical model with experimental data (see Methods for details). Based on the observation that the myo-II cable detachment occurred at $L_0 \approx 0.4$ μm in *WT* cells, we estimated $(\gamma, \gamma') \approx (6\sigma, 4\sigma)$. The changes in the myo-II and Jub signal intensities at the shrinking AP junctions (Fig. 2j, Fig. 4f) suggest that the initial value of γ is below 3σ, with which the system is in the attached region at $\theta = 60°$ and $L_0 > 0.4$ μm. Therefore, using the *WT* parameter values, cortical myo-II cables can be attached to the non-remodeling junction. After the short remodeling junctions were reconnected, θ' was approximately $50°$ at the time of rsMC fission (Fig. 4e). Substituting $\theta' = 50°$, $L_0' = 0.4$ μm, and $(\gamma, \gamma') = (6\sigma, 4\sigma)$ into the condition equation for the detached state (II) indicates that the system resides at the boundary between the detached and attached states (Fig. 4j). Considering the decrease in the myo-II signal intensity along the horizontal edges of the rsMC (Fig. 1e) and the increase in L_0' by the junction elongation, the parameter values are changed as $(\gamma, \gamma') \approx (6\sigma, 3\sigma)$ and $L_0' \approx 0.6$ μm. With the updated parameter values, a retransition from the detached state to the attached state is induced (Fig. 4j). These

results suggest that the transition between the attached and detached states is possible using the estimated *in vivo* parameters.

In summary, the theoretical analysis of the minimal mechanical model elucidates how the physical properties of cortical myo-II cables are integrated with the junction geometry to govern their dewetting/wetting behaviors during cell rearrangement.

Pten lowers tension of myo-II cables to induce its reattachment to the junction

To further clarify how temporal changes in tension affect the reattachment of myo-II cables to the junction, we analyzed *phosphatase and tensin homolog* (*pten*) RNAi cells. In the *Drosophila* wing, PTEN is responsible for lowering the levels of phosphatidylinositol (3,4,5)-triphosphate and myo-II at the PD junctions after junction exchange, leading to the elongation of newly generated PD junctions[29]. We found that myo-II levels were elevated and the reduction in myo-II levels at the horizontal (PD) edges of the rsMC was suppressed in *pten* RNAi cells (Fig. 5a). Under such conditions, the myo-II cables could not attach to the AJ (Fig. 5b–e, Supplementary Video 7). The comparison of the myo-II signal intensity between *WT* and *pten* RNAi cells yielded estimates of the ratio of cable's tension and adhesion $(\gamma, \gamma') \approx (9\sigma, 7\sigma)$ (see Methods for details). Substituting the estimated parameter values into the condition equation for the detached state (II) confirmed that reattachment was prohibited in *pten* RNAi cells. These results further supported the validity of the proposed mechanical model.

Discussion

This study delineates the mechanism by which junctions are exchanged in epithelial cells (Fig. 6). The size and duration time of multicellular myo-II cables are autonomously coordinated through the junction geometry and mechanics to loosen the junctional structure locally and transiently. The transient formation of the rsMC may prevent dilution of DE-cad at loosened junctions as suggested by the decrease of DE-cad signal at long-lasting rsMCs (magenta arrowheads in Fig. 2a). In addition, the directional information of the shrinking junction is inherited by the differential myo-II accumulation along the vertical and horizontal edges of the rsMC, which ensures unidirectional cell rearrangement by inducing the reattachment to junctions along edges with lower myo-II levels. This represents an advantage of the rsMC–mediated mechanism over *in situ* regulation at cell–cell contact surfaces in supporting the fidelity of junction exchange.

M6 is not detected in immature epithelial cells, including germband cells, and cells start to express M6 as the epithelium matures[12]. Thus, immature epithelial cells such as germband cells may deform cell membranes via actin-rich basolateral protrusions to form a multicellular rosette[7]. In contrast, mature epithelial cells such as pupal wing cells may reconnect junctions at more apical sides via M6. The mechanism whereby M6 regulates AJ components such as Jub in wing cells (this study) and Cno in Ras^{V12}-overexpressing eye disc cells[23] remains unclear. Since the mammalian homologue of M6 is involved in the actin regulation[25,30], M6 may control actin remodeling, which is known to affect the structure and dynamics of AJ[16,19,31]. Alternatively, M6 may directly interact with the AJ components through a rapid, short-term translocation to the AJ, as the position of junction compartments can dynamically change during the development[32]. More experiments such as simultaneous tracking of the AJ and SJ components[24,26] will be necessary to elucidate how AJ and SJ interact and coordinate during junction exchange.

We introduced a simple theoretical model and uncovered the mechanical and geometrical conditions under which cortical myo-II cables attach to and detach from the junctional membrane. These conditions are compatible with the temporal changes in myo-II and jub levels in *WT* and RNAi cells. However, our model considers only the static force balance and thus cannot describe the entire process of junction exchange. To understand the dynamics of junction exchange, a more comprehensive model, including the turnover of actomyosin and junction components, needs to be developed. Recently, Nestor-Bergmann et al. proposed the Apposed-Cortex Adhesion Model, which investigates how the duration of cell-cell membrane linkage at the molecular scale affects cell rearrangement[33]. Extending our model to incorporate the concept of Apposed-Cortex Adhesion Model is an interesting direction for future research.

In conclusion, the present study shed light on the orchestration of geometry, mechanics and signaling around the cell vertex for reconnection of junctions. The

363 proposed mechanism can potentially contribute to other aspects of morphogenesis. For
364 instance, the rsMC-like structure at the vertex of a non-remodeling junction implies its
365 relevance in a ratchet-like movement of the vertex along the junction[13]. In addition,
366 because loss-of-function of M6 causes excess extrusion of cancer cells[23], it is possible
367 that M6 and actin-AJ linkers function to sense the risk of fracture at cell vertices,
368 thereby preventing the formation of wounds in the epithelium. Given recent findings
369 on the reorganization of the cytoskeleton and information sensing at the cell
370 vertex[8,9,13,15,34,35], further dissecting the complex interplay between actin-AJ regulators,
371 TCJ proteins, and the geometry and mechanics at the vertices will clarify the origin of
372 collective cell behaviors in epithelial development and plasticity.
373
374

375 # STAR Methods

376

377 ## KEY RESOURCES TABLE

REAGENT or RESOURCE	SOURCE	IDENTIFIER
Experimental models: *Drosophila melanogaster* strains		
DE-cad-GFP	From Yang Hong [36]	N/A
DE-cad-mTagRFP	From Yohanns Bellaïche [37]	N/A
sqhp-sqh-GFP	From Roger Karess [38]	N/A
sqhp-sqh-mKate2×3	From Yohanns Bellaïche [37]	N/A
dlg-GFP	Bloomington *Drosophila* Stock Center	BDSC #50859
UAS-lifeact-GFP	Bloomington *Drosophila* Stock Center	BDSC #35544
cno-YFP	Kyoto stock center	DGRC #115111
jub-GFP	Bloomington *Drosophila* Stock Center	BDSC #56806
vinc-GFP	From Yohanns Bellaïche [37]	N/A
flr-GFP	Bloomington *Drosophila* Stock Center	BDSC #50824
tsr-GFP	From [42]	N/A
ubi-Da-cat-GFP	From [43], [44]	N/A
UAS-Da-cat-TagRFP	From [45]	N/A
m6-GFP	From María Fernanda Ceriani [39]	N/A
sdk-YFP	Kyoto Stock Center	DGRC #115049
aka-GFP	From [46]	N/A
ptc-Gal4	Bloomington *Drosophila* Stock Center	BDSC #2017
MS1096-Gal4	Bloomington *Drosophila* Stock Center	BDSC #8860
tub-Gal80^{ts}	Bloomington *Drosophila* Stock Center	BDSC #7108
Ay-Gal4	Kyoto Stock Center	DGRC #107529
hs-Flp	From Kei Ito [47]	N/A
UAS-jub dsRNA	Bloomington *Drosophila* Stock Center	BDSC #32923
UAS-cno dsRNA	National Institute of Genetics	NIG #2534R-2
UAS-vinc dsRNA	National Institute of Genetics	NIG #3299R-2
UAS-Dα-cat dsRNA	Vienna *Drosophila* Resource Center	VDRC #19182
UAS-flr dsRNA	Vienna *Drosophila* Resource Center	VDRC #108442
UAS-tsr dsRNA	Vienna *Drosophila* Resource Center	VDRC #110599
UAS-m6 dsRNA	National Institute of Genetics	NIG #7540R-2

UAS-sdk dsRNA	Bloomington *Drosophila* Stock Center	BDSC #33412
UAS-aka dsRNA	Bloomington *Drosophila* Stock Center	BDSC #67014
UAS-pten dsRNA	Bloomington *Drosophila* Stock Center	BDSC #33643
UAS-mCD8-GFP	Kyoto Stock Center	DGRC #108068
Software and algorithms		
ImageJ Software	National Institute of Health, USA	https://imagej.nih.gov/ij/
R	The R Project for Statistical Computing	https://www.r-project.org/
Anaconda	Anaconda Distribution	https://www.anaconda.com/
EZR	Jichi Medical University Saitama Medical Center	http://www.jichi.ac.jp/saitama-sct/SaitamaHP.files/statmedEN.html
Python	The Python Programming Language	https://www.python.org/
Others		
An inverted confocal microscope (Nikon A1R)	Nikon	https://www.microscope.healthcare.nikon.com/products/confocal-microscopes
A confocal microscope (Zeiss LSM900)	Zeiss	https://www.zeiss.com/microscopy/int/products/confocal-microscopes.html
An inverted confocal spinning disk microscope (Olympus IX83 combined with Yokogawa CSU-W1)	Olympus Yokogawa	https://www.olympus-lifescience.com/en/microscopes/inverted/ix83/ https://www.yokogawa.com/eu/solutions/products-platforms/life-science/spinning-disk-confocal/csu-w1-confocal-scanner-unit/
A high-speed confocal platform (Nikon ECLIPSE Ti2 combined with Dragonfly 500)	Nikon Andor	https://www.microscope.healthcare.nikon.com/products/inverted-microscopes/eclipse-ti2-series https://andor.oxinst.com/products/dragonfly-confocal-microscope-system
iXon3 888 EMCCD camera	Andor	https://andor.oxinst.com/products/ixon-emccd-cameras-for-life-science
Zyla sCMOS camera	Andor	https://andor.oxinst.com/products/scmos-camera-series/zyla-4-2-scmos

382 **RESOURCE AVAILABILITY**

383 **Lead contact**

384 Further information and requests for resources and reagents should be directed to and
385 will be fulfilled by the lead contact, Kaoru Sugimura (sugimura@bs.s.u-tokyo.ac.jp).

386

387 **Materials availability**

388 This study did not generate new unique reagents.

389

390 **Data and code availability**

391 The authors declare that the data supporting the findings of this study are available
392 within the paper and its Supplementary files. The data are available from the
393 corresponding authors upon reasonable request.

394

395 **EXPERIMENTAL MODEL AND SUBJECT DETAILS**

396 ***Drosophila* genetics**

397 *Drosophila* stocks were maintained at 25°C or 17°C. The flies used in the present study
398 were *DE-cad-GFP*[36], *DE-cad-mTagRFP*[37], *sqhp-sqh-GFP*[38], *sqhp-sqh-mKate2×3*[37],
399 *dlg-GFP* (Flytrap #YC0005)[39], *UAS-lifeact-GFP* (Bloomington Stock Center #35544),
400 *cno-YFP* (Flytrap #CPTI-000590)[40], *jub-GFP*[41], *vinc-GFP*[37], *flr-GFP* (Flytrap
401 #CA07499)[39], *tsr-GFP* (Flytrap #ZCL0613)[42], *ubi-Dα-cat-GFP*[43,44], *UAS-Dα-cat-*
402 *TagRFP*[45], *m6-GFP* (Flytrap #CA06602)[39], *sdk-YFP* (Flytrap #CPTI000812)[40], *aka-*
403 *GFP*[46], *UAS-mCD8-GFP* (Kyoto Stock Center #108068)[22], *ptc-Gal4* (Bloomington
404 Stock Center #2017), *MS1096-Gal4* (Bloomington Stock Center #8860), *tub-Gal80*^{ts}
405 (Bloomington Stock Center #7108), *Ay-Gal4* (Kyoto Stock Center #107529), *hs-Flp*[47],
406 *UAS-jub dsRNA* (Bloomington Stock Center #32923), *UAS-cno dsRNA* (NIG-Fly
407 #2534R-2), *UAS-vinc dsRNA* (NIG-Fly #3299R-2), *UAS-Dα-cat dsRNA* (VDRC
408 #19182), *UAS-flr dsRNA* (VDRC #108442), *UAS-tsr dsRNA* (VDRC #110599), *UAS-*
409 *m6 dsRNA* (NIG-Fly #7540R-2), *UAS-sdk dsRNA* (Bloomington Stock Center #33412),
410 *UAS-aka dsRNA* (Bloomington Stock Center #67014), and *UAS-pten dsRNA*
411 (Bloomington Stock Center #33643). The list of genotypes and crossing conditions are
412 summarized in Genotypes of the experimental model.

413 To generate a mosaic clone expressing Lifeact-GFP, heat shock activated flip-
414 out-Gal4-UAS system was used[47]. *hs-Flp*; *Ay-Gal4* females were crossed to *sqhp-sqh-*
415 *mKate2×3*, *UAS-Lifeact-GFP* males at 25°C overnight. After the vial had been
416 maintained for four days, heat-shock at 37°C was performed for 90 min. White pupae
417 were then picked up and observed at 24 or 25 h APF.

418

419 **Genotypes of the experimental model**

420 Genotypes used for each figure are listed including temperature and hours after
421 puparium formation.

422

	Genotype	Culture condition (Observation time point)
Fig. 1	*sqh^{AX3}/sqh^{AX3}* or *Y*; *sqhp-sqh-GFP*	White pupae were picked up and observed at 25°C. (25 h APF)
	sqhp-sqh-mKate2×3, DE-cad-GFP/DE-cad-GFP	White pupae were picked up and observed at 25°C. (25 h APF)
	ptc-Gal4, sqhp-sqh-mKate2×3/UAS-mCD8-GFP	Crossed at 17°C. White pupae were picked up and observed at 25°C. (24 h APF)
	DE-cad-mTagRFP, sqhp-sqh-GFP/DE-cad-mTagRFP	White pupae were picked up and observed at 25°C. (24 h APF)
	dlg-GFP/+ or *Y*; *sqhp-sqh-mKate2×3/+*	White pupae were picked up and observed at 25°C. (24 h APF)
	sdk-YFP/+ or *Y*; *sqhp-sqh-mKate2×3/+*	White pupae were picked up and observed at 25°C. (25 h APF)
Fig. 2	*sqhp-sqh-mKate2×3, DE-cad-GFP/DE-cad-GFP*	White pupae were picked up and observed at 25°C. (25 h APF)
	ptc-Gal4, DE-cad-GFP, sqhp-sqh-mKate2×3/DE-cad-GFP; *UAS-jub dsRNA/+*	Crossed at 17°C. White pupae were picked up and observed at 25°C. (25 h APF)
	ptc-Gal4, DE-cad-GFP, sqhp-sqh-mKate2×3/DE-cad-GFP; *UAS-cno dsRNA/+*	Crossed at 17°C. White pupae were picked up and observed at 25°C. (25 h APF)
	ptc-Gal4, DE-cad-GFP, sqhp-sqh-mKate2×3/DE-cad-GFP; *UAS-Dα-cat dsRNA/+*	Crossed at 17°C. White pupae were picked up and observed at 25°C. (25 h APF)
	ptc-Gal4, DE-cad-GFP, sqhp-sqh-mKate2×3/DE-cad-GFP, UAS-vinc dsRNA	White pupae were picked up and observed at 25°C. (25 h APF)
	ptc-Gal4, sqhp-sqh-mKate2×3/UAS-mCD8-GFP; *UAS-jub dsRNA/+*	Crossed at 17°C. White pupae were picked up and observed at 25°C. (24 h APF)
	sqhp-sqh-mKate2×3/+; *jub-GFP/+*	White pupae were picked up and observed at 25°C. (25 h APF)
Fig. 3	*DE-cad-mTagRFP, sqhp-sqh-GFP/DE-cad-mTagRFP*	White pupae were picked up and observed at 25°C. (24 h APF)
	sqhp-sqh-mKate2×3, DE-cad-GFP/DE-cad-GFP	White pupae were picked up and observed at 25°C. (25 h APF)
	MS1096-Gal4/+ or *Y*; *sqhp-sqh-mKate2×3, DE-cad-GFP/DE-cad-GFP*; *UAS-m6 dsRNA/+*	White pupae were picked up and observed at 25°C. (25 h APF)
	ptc-Gal4, DE-cad-GFP, sqhp-sqh-mKate2×3/DE-cad-GFP, UAS-aka dsRNA	White pupae were picked up and observed at 25°C. (25 h APF)
	ptc-Gal4, DE-cad-GFP, sqhp-sqh-mKate2×3/+; *UAS-sdk dsRNA/+*	White pupae were picked up and observed at 25°C. (25 h APF)
	MS1096-Gal4/+ or *Y; sqhp-sqh-mKate2×3/+*; *jub-GFP, UAS-m6 dsRNA/+*	White pupae were picked up and observed at 25°C. (24 h APF)

	sqhp-sqh-mKate2×3/+; *m6-GFP/+*	White pupae were picked up and observed at 25°C. (24 h APF)
	ptc-Gal4, sqhp-sqh-mKate2×3/UAS-aka dsRNA; *m6-GFP/+*	White pupae were picked up and observed at 25°C. (24 h APF)
	sqhp-sqh-mKate2×3/aka-GFP	White pupae were picked up and observed at 25°C. (24 h APF)
	MS1096-Gal4/+ or *Y*; *sqhp-sqh-mKate2×3/aka-GFP*; *UAS-m6 dsRNA/+*	White pupae were picked up and observed at 25°C. (24 h APF)
	DE-cad-mTagRFP /+; *m6-GFP/+*	White pupae were picked up and observed at 25°C. (24 h APF)
	ptc-Gal4, DE-cad-mTagRFP/+; *m6-GFP/UAS-jub dsRNA*	Crossed at 17°C. White pupae were picked up and observed at 25°C. (24 h APF)
Fig. 4	*sqhp-sqh-mKate2×3, DE-cad-GFP/DE-cad-GFP*	White pupae were picked up and observed at 25°C. (25 h APF)
Fig. 5	*sqhp-sqh-mKate2×3, DE-cad-GFP/DE-cad-GFP*	White pupae were picked up and observed at 25°C. (25 h APF)
	ptc-Gal4, DE-cad-GFP, sqhp-sqh-mKate2×3/DE-cad-GFP; *UAS-pten dsRNA/+*	Crossed at 17°C. White pupae were picked up and observed at 25°C. (25 h APF)
Supplementary Fig. 1	*sqhp-sqh-mKate2×3, DE-cad-GFP/DE-cad-GFP*	White pupae were picked up and observed at 25°C. (25 h APF)
	hs-Flp/+ or *Y*; *Ay-Gal4/sqhp-sqh-mKate2×3, UAS-lifeact-GFP*	Crossed at 25°C. 4 days later, heat shock was performed at 37°C for 90 min and cultured at 17°C. White pupae were picked up and observed at 25°C. (25 h APF)
Supplementary Fig. 2	*ptc-Gal4, sqhp-sqh-mKate2×3/+*; *UAS-jub dsRNA/jub-GFP*	Crossed at 17°C. White pupae were picked up and observed at 25°C. (24 h APF)
	ptc-Gal4, sqhp-sqh-mKate2×3/+; *UAS-cno dsRNA/cno-YFP*	Crossed at 17°C. White pupae were picked up and observed at 25°C. (24 h APF)
	ptc-Gal4, sqhp-sqh-mKate2×3/+; *ubi-Dα-cat-GFP/UAS-Dα-cat dsRNA*	Crossed at 17°C. White pupae were picked up and observed at 25°C. (24 h APF)
	vinc-GFP/+ or *Y*; *ptc-Gal4, sqhp-sqh-mKate2×3/UAS-vinc dsRNA*	White pupae were picked up and observed at 25°C. (24 h APF)
	ptc-Gal4, aka-GFP/UAS-aka dsRNA	White pupae were picked up and observed at 25°C. (24 h APF)
	sdk-GFP/+ or *Y*; *ptc-Gal4, sqhp-sqh-mKate2×3/+*; *UAS-sdk dsRNA/+*	White pupae were picked up and observed at 25°C. (24 h APF)
	sqhp-sqh-mKate2×3/+; *m6-GFP/+*	White pupae were picked up and observed at 25°C. (24 h APF)
	MS1096-Gal4/+ or *Y*; *sqhp-sqh-mKate2×3/+*; *m6-GFP, UAS-m6 dsRNA/+*	White pupae were picked up and observed at 25°C. (24 h APF)

Supplementary Fig. 3	*sqhp-sqh-mKate2×3, DE-cad-GFP/DE-cad-GFP*	White pupae were picked up and observed at 25°C. (25 h or 32h APF)
	ptc-Gal4, DE-cad-GFP, sqhp-sqh-mKate2×3/DE-cad-GFP; *UAS-jub dsRNA/+*	Crossed at 17°C. White pupae were picked up and observed at 25°C. (25 h or 32h APF)
	ptc-Gal4, DE-cad-GFP, sqhp-sqh-mKate2×3/DE-cad-GFP; *UAS-cno dsRNA/+*	Crossed at 17°C. White pupae were picked up and observed at 25°C. (25 h or 32h APF)
	ptc-Gal4, DE-cad-GFP, sqhp-sqh-mKate2×3/DE-cad-GFP; *UAS-Dα-cat dsRNA/+*	Crossed at 17°C. White pupae were picked up and observed at 25°C. (25 h or 32h APF)
	ptc-Gal4, DE-cad-GFP, sqhp-sqh-mKate2×3/DE-cad-GFP, UAS-vinc dsRNA	White pupae were picked up and observed at 25°C. (25 h or 32h APF)
	sqhp-sqh-mKate2×3/+; *cno-YFP/+*	White pupae were picked up and observed at 25°C. (25 h APF)
	sqhp-sqh-mKate2×3/+; *ubi-Dα-cat-GFP/+*	White pupae were picked up and observed at 25°C. (25 h APF)
Supplementary Fig. 4	*sqhp-sqh-mKate2×3/+*; *cno-YFP/+*	White pupae were picked up and observed at 25°C. (24 h APF)
	ptc-Gal4, sqhp-sqh-mKate2×3/+; *UAS-jub dsRNA/cno-YFP*	Crossed at 17°C. White pupae were picked up and observed at 25°C. (24 h APF)
	ptc-Gal4, sqhp-sqh-mKate2×3/UAS-vinc dsRNA; *cno-YFP/+*	White pupae were picked up and observed at 25°C. (24 h APF)
	ptc-Gal4, sqhp-sqh-mKate2×3/+; *UAS-Dα-cat dsRNA/cno-YFP*	Crossed at 17°C. White pupae were picked up and observed at 25°C. (24 h APF)
	sqhp-sqh-mKate2×3/+; *jub-GFP/+*	White pupae were picked up and observed at 25°C. (24 h APF)
	ptc-Gal4, sqhp-sqh-mKate2×3/+; *UAS-cno dsRNA/jub-GFP*	Crossed at 17°C. White pupae were picked up and observed at 25°C. (24 h APF)
	ptc-Gal4, sqhp-sqh-mKate2×3/UAS-vinc dsRNA; *jub-GFP/+*	White pupae were picked up and observed at 25°C. (24 h APF)
	ptc-Gal4, sqhp-sqh-mKate2×3/+; *UAS-Dα-cat dsRNA/jub-GFP*	Crossed at 17°C. White pupae were picked up and observed at 25°C. (24 h APF)
	vinc-GFP/+ or *Y*; *sqhp-sqh-mKate2×3/+*	White pupae were picked up and observed at 25°C. (24 h APF)
	vinc-GFP/+ or *Y*; *ptc-Gal4, sqhp-sqh-mKate2×3/+*; *UAS-jub dsRNA/+*	Crossed at 17°C. White pupae were picked up and observed at 25°C. (24 h APF)
	vinc-GFP/+ or *Y*; *ptc-Gal4, sqhp-sqh-mKate2×3/+*; *UAS-cno dsRNA/+*	Crossed at 17°C. White pupae were picked up and observed at 25°C. (24 h APF)

	vinc-GFP/+ or *Y*; *ptc-Gal4, sqhp-sqh-mKate2×3/+*; *UAS-Dα-cat dsRNA/+*	Crossed at 17°C. White pupae were picked up and observed at 25°C. (24 h APF)
	sqhp-sqh-mKate2×3/+; *ubi-Dα-cat-GFP/+*	White pupae were picked up and observed at 25°C. (25 h APF)
	ptc-Gal4, sqhp-sqh-mKate2×3/+; *ubi-Dα-cat-GFP/UAS-jub dsRNA*	Crossed at 17°C. White pupae were picked up and observed at 25°C. (24 h APF)
	ptc-Gal4, sqhp-sqh-mKate2×3/+; *ubi-Dα-cat-GFP/UAS-cno dsRNA*	Crossed at 17°C. White pupae were picked up and observed at 25°C. (24 h APF)
	ptc-Gal4, sqhp-sqh-mKate2×3/UAS-vinc dsRNA; *ubi-Dα-cat-GFP/ +*	White pupae were picked up and observed at 25°C. (24 h APF)
Supplementary Fig. 5	*ptc-Gal4, sqhp-sqh-mKate2×3/UAS-flr dsRNA*; *jub-GFP/+*	White pupae were picked up and observed at 17°C. (58 h APF at 17°C)
	ptc-Gal4, sqhp-sqh-mKate2×3, tub-Gal80^{ts}/UAS-tsr dsRNA; *jub-GFP/+*	Crossed at 21°C. During the 3rd instar stage, temperature was shifted up at 29°C. After 20-22 h, white pupae were picked up and observed at 29°C. (20.5 h APF at 29°C)
	sqhp-sqh-mKate2×3; *flr-GFP*	White pupae were picked up and observed at 25°C. (24 h APF)
	ptc-Gal4, UAS-Dα-cat-TagRFP/tsr-GFP	Crossed at 17°C. White pupae were picked up and observed at 25°C. (24 h APF)
	sqhp-sqh-mKate2×3/+; *m6-GFP/+*	White pupae were picked up and observed at 25°C. (24 h APF)
	ptc-Gal4, sqhp-sqh-mKate2×3/UAS-flare dsRNA; *m6-GFP/+*	White pupae were picked up and observed at 17°C. (58 h APF at 17°C)
	ptc-Gal4, sqhp-sqh-mKate2×3/tub-Gal80^{ts},UAS-tsr dsRNA; *m6-GFP/+*	Crossed at 21°C. During the 3rd instar stage, temperature was shifted up at 29°C. After 20-22 h, white pupae were picked up and observed at 29°C. (20.5 h APF at 29°C)
	ptc-Gal4, DE-cad-GFP, sqhp-sqh-mKate2×3/DE-cad-GFP, UAS-aka dsRNA	White pupae were picked up and observed at 25°C. (25 h APF)
	ptc-Gal4, DE-cad-GFP, sqhp-sqh-mKate2×3/+; *UAS-sdk dsRNA/+*	White pupae were picked up and observed at 25°C. (25 h APF)
	sqhp-sqh-mKate2×3/aka-GFP	White pupae were picked up and observed at 25°C. (24 h APF)
	ptc-Gal4, sqhp-sqh-mKate2×3/aka-GFP; UAS-jub dsRNA/+	Crossed at 17°C. White pupae were picked up and observed at 25°C. (24 h APF)
	sdk-YFP/+ or *Y*; *sqhp-sqh-mKate2×3/+*	White pupae were picked up and observed at 25°C. (24 h APF)

	sdk-YFP/+ or *Y; ptc-Gal4, sqhp-sqh-mKate2×3/+*; *UAS-jub dsRNA /+*	Crossed at 17°C. White pupae were picked up and observed at 25°C. (24 h APF)

METHOD DETAILS

Image collection

The preparation of *Drosophila* pupal wing samples for image collection was carried out as previously described[45,48,49]. In brief, pupae at appropriate ages were dissected to remove the pupal case on top of the left wing and were placed on a small drop of Immersol W 2010 (Zeiss 444969-0000-000) in a glass bottom dish. The fixed time-point images and cross section images shown in Fig. 1g–k, Supplementary Fig. 1b–g, i, j, and 5e were acquired using an inverted confocal microscope (A1R; Nikon) equipped with a 60×/NA1.2 Plan Apochromat water-immersion objective at room temperature. Low-magnification images of the wing shown in Supplementary Fig. 3c–g were acquired using a confocal microscope (LSM 900; Zeiss) equipped with a 10×/NA0.45 Plan Apochromat objective (Zeiss) at room temperature. The time-lapse images shown in Supplementary Fig. 5c were acquired at 25°C using an inverted confocal spinning disk microscope (Olympus IX83 combined with Yokogawa CSU-W1) equipped with an iXon3 888 EMCCD camera (Andor), an Olympus 100×/NA1.35 SplanApo silicone oil-immersion objective, and a temperature control chamber (TOKAI HIT), using IQ 2.9.1 (Andor)[49]. Images in other figures were acquired using a high-speed confocal platform, Dragonfly (Nikon ECLIPSE Ti2 combined with Dragonfly 500 unit) equipped with an Zyla sCMOS camera (Andor), a 60×/NA1.20 CFI Plan Apochromat VC water-immersion objective (Nikon), using Fusion (Andor). After imaging, we confirmed that the pupae survived to at least the pharate stage.

Surgical manipulation to relax the tissue stretch

To analyze the effects of tissue tension on cell rearrangement (Supplementary Fig. 1f–h), wings were detached from the hinges using forceps. Details were described previously[16, 48]. Briefly, before removing pupal case, hinges were severed at 23.5–24 h APF by rubbing forceps on hinge region. Pupal cases were then removed, pupae were mounted on glass bottom dishes as described image collection section.

QUANTIFICATION AND STATISTICAL ANALYSIS

Image analysis

We focused on the rsMC generated from the AP junctions but not from the PD junctions. To quantify the area of the rsMC, the inner perimeter of the rsMC was manually tracked using the region of interest (ROI) manager in ImageJ. The junction length and the half-angle between connecting junctions were measured using line and angle tools, respectively, in ImageJ.

461 Z-projection was performed to extract the fluorescent signals on the AJ or SJ
462 planes. The background signal of myo-II-mKate2 or DE-cad-GFP was subtracted using
463 the 'subtract background' command ($r = 50$; except Supplementary Fig. 5d, see below),
464 and the signal intensity was measured by manually selecting ROIs and using the ROI
465 manager in ImageJ. The rsMC was divided into four edges (v_1, v_2, h_1, and h_2), as shown
466 in Fig. 1d. In Fig. 1e and 5a, the spatial myo-II-mKate2 signal intensities at the rsMC
467 were calculated using 'Plot Profile' in ImageJ with a line width of 10 pixel. In Fig. 2j
468 and 3g, to measure the signal intensities of Jub-GFP, the background signal was
469 subtracted using the 'subtract background' command ($r = 100$), and the signal intensity
470 was quantified using 'Plot Profile' in ImageJ with a line width of 5 pixel. In
471 Supplementary Fig. 5d, to measure the signal intensities of AIP1-GFP and myo-II-
472 mKate2, the background signal was subtracted using the 'subtract background'
473 command ($r = 100$), and the signal intensity was quantified using 'Plot Profile' in
474 ImageJ with a line width of 7 pixel.,
475
476 **Statistics**
477 P-values were calculated in R or Python based on the Mann-Whitney *U* test (Fig. 1d),
478 the Steel-Dwass test (Fig. 2c, d, h, Fig. 3c, d, Fig. 5c, d, Supplementary Fig. 1c, d, f, g,
479 Supplementary Fig. 3a), the Student's *t*-test (Fig. 2j), the Welch's *t*-test (Fig. 3g), the
480 correlation analysis (Fig. 2g, Supplementary Fig. 1i, j), and the paired *t*-test (Fig. 4e).
481 The Steel-Dwass test was performed when comparing every pair in all groups. The
482 Mann-Whitney *U* test, the Steel-Dwass test, the Student's *t*-test, and the Welch's *t*-test
483 were performed with EZR (Saitama Medical Center, Jichi Medical University, Saitama,
484 Japan, https://www.jichi.ac.jp/saitama-sct/SaitamaHP.files/statmed.html), which is a
485 graphical user interface for R (The R Foundation for Statistical Computing, Vienna,
486 Austria)[50]. More precisely, it is a modified version of R commander designed to add
487 statistical functions frequently used in biostatistics. The correlation analysis and paired
488 *t*-test were performed with SciPy module in Python.
489
490 **MODELING**
491 **Mechanical model of the junction exchange**
492 ***Model construction and analysis***
493 We constructed a mechanical model of the cortical myo-II cables immediately before,
494 during, and after the junction exchange. We considered the free energy, which consists
495 of the tensile energy of the myo-II cables and the adhesive energy between the myo-II
496 cables and junction. The underlying assumption is that the relaxation of tension and
497 adhesion between myosin cables and AJ components is faster than the cell reconnection
498 time (~10 min) and rsMC dynamics (~5 min). Given that the lifetime of the binding of
499 actin–AJ linkers to actin cytoskeleton to of the order of 1–10 s[51], this assumption is
500 valid for the situation considered here.

We assumed that detached myo-II cables maintain a rectangular shape and set up a symmetrical geometry for the sake of simplicity (Fig. 4a, b). Quantification of the junction geometry showed that the length of vertical remodeling junction L_0 is approximately 0.4 μm (Fig. 4c). l is the length of the connecting junctions, from which cortical myo-II is detached. Since l was too small to measure precisely, we used an approximate value $l \approx 0.2$ μm. Due to limitations in image resolution, the myo-II signals along the vertical remodeling junction and at the 0.2 μm-end of connection junctions could not be separated. We thus assume that the tension of myo-II cables does not change at the 0.2 μm-end of connection junctions.

The free energies of the attached and detached states (F_a and F_d) are originated from the cable's tension and adhesion to the junction, whose energies per unit length are γ and $-\sigma$, respectively. The detachment of cortical myo-II cables is conditioned by $F_d - F_a < 0$. Before the vertical, AP junction is reconnected, the difference in the free energies of attached and detached (I) states are $F_d - F_a = -4\gamma l(1-\cos\theta) - 4\gamma' l(1-\sin\theta) + 2\sigma(L_0 + 4l)$. This leads to the condition equation for the detachment $\gamma(1-\cos\theta) + \gamma'(1-\sin\theta) > \sigma(2 + L_0/2l)$ (Fig. 4i, black line). After the reconnection of junctions, the reattachment is favored when $\gamma(1-\cos\theta') + \gamma'(1-\sin\theta') < \sigma(2 + L_0'/2l)$ is satisfied, where γ' is the tension of horizontal edges of the rsMC (Fig. 4j, black line).

Evaluation of model parameters

Following the data presented in Fig. 4c, we set $L_0 = 0.4$ in Fig. 4g–j. The half-angle between the connecting junctions (θ) was approximately $60°$ at the time of the rsMC formation (Fig. 4d). Quantification of the change in θ during junction shrinkage (Fig. 4e) suggests that the change in junction angle is not the main trigger of myo-II detachment. After junction reconnection, as the newly generated junction elongates, θ' decreases, as shown in Fig. 4e. Based on these results, we treated θ and θ' as constants in the main text: $\theta = 60°$ for Fig. 4g–i, and $\theta' = 50°$ for Fig. 4j.

Experimental data showed that the ratio of myo-II-mKate2 signal intensity was $\sim 3:2$ for the vertical and horizontal edges of rsMC at the time of rsMC formation (Fig. 1d) and that the myo-II cable detachment occurred at $L_0 \approx 0.4$ μm (Fig. 2c). By substituting $\gamma = (3/2)\gamma'$ and *in vivo* geometrical parameters into the condition equation for the detached state (I) in Fig. 4b, we estimated $(\gamma, \gamma') \approx (6\sigma, 4\sigma)$ at the time point of rsMC formation (white circle in Fig. 4i). We use this value as a reference for parameter estimation. During the shrinkage of AP junctions, the myo-II signal intensity approximately doubled and the Jub signal intensity decreased by approximately 20% (Fig. 2j, Fig. 4f). Thus, we estimate that γ is initially below 3σ, with which the system is in the attached region at $\theta = 60°$ and $L_0 > 0.4$ (Fig. 4h, i). During the junction exchange, the myo-II signal intensity along the horizontal edges of the rsMC dropped by approximately 20%, whereas that along the vertical edges remained unchanged (Fig. 1e). This observation provides the estimates of $(\gamma, \gamma') \approx$

$(6\sigma, 3\sigma)$ (gray circle in Fig. 4j). In addition, the length of the newly generated PD junction, L_0' is increased during cell rearrangement. With $(\gamma, \gamma') \approx (6\sigma, 3\sigma)$ and $L_0' = 0.6\,\mu m$, the re-attached state is favored energetically (Fig. 4j). We estimated model parameters in RNAi cells in the same procedure. Based on the myo-II signal intensity (magenta line in Fig. 5a), we estimated $(\gamma, \gamma') \approx (9\sigma, 7\sigma)$ in *pten* RNAi cells. With these parameters, the reattachment of myo-II cables is prohibited even at $L_0 = 0.6$ (Fig. 4j).

Acknowledgments

The authors would like to thank Yohanns Bellaïche, Yang Hong, Roger Kares, María Fernanda Ceriani, the Bloomington Stock Center, the Kyoto Stock Center, the Vienna *Drosophila* Resource Center (VDRC), NIG-Fly, the *Drosophila* Genomics Resource Center, and the Developmental Studies Hybridoma Bank for reagents; Goshi Ogita, Miho Aruga, Kyoko Komano, and Risa Matsui for technical assistance; the iCeMS Analysis Center, Shizue Ohsawa, and the Nagoya University Live Imaging Center for imaging equipment; and Tetsuhisa Otani and Yohanns Bellaïche for critical reading of the manuscript. This study was financially supported by JSPS KAKENHI Grant (17K15125), the AMED PRIME program (20gm5810025h9904), the Sumitomo Foundation (200303), and the Takeda Science Foundation to K.S., JSPS KAKENHI Grant (19K16139) and The Uehara Memorial Foundation (202110172) to K.I., JST CREST (JPMJCR1923) to S.I., and JSPS KAKENHI Grant (18KK0234) to Y.T.

Author contributions

K.I. and K.S. designed the research. K.I. performed the experiments. Y.T. assisted the experiments. K.I., K.S and S.I. analyzed the data. S.I. constructed and analyzed mathematical model with input from K.S. K.S., K.I. and S.I. drafted the manuscript. All authors approved the final manuscript.

Competing interests

The authors declare no competing interests.

References

1. Lecuit, T. (2005). Adhesion remodeling underlying tissue morphogenesis. Trends Cell Biol. *15*, 34–42.
2. Takeichi, M. (2014). Dynamic contacts: rearranging adherens junctions to drive epithelial remodelling. Nat. Rev. Mol. Cell Biol. *15*, 397–410.
3. Pinheiro, D., and Bellaïche, Y. (2018). Mechanical Force-Driven Adherens Junction Remodeling and Epithelial Dynamics. Dev. Cell *47*, 3-19.
4. Sutherland, A., Keller, R., and Lesko, A. (2020). Convergent extension in mammalian morphogenesis. Semin. Cell Dev. Biol. *100*, 199–211.
5. Lemke, S.B., and Nelson, C.M. (2021). Dynamic changes in epithelial cell packing during tissue morphogenesis. Curr. Biol. *31*, R1098–R1110.
6. Heer, N.C., and Martin, A.C. (2017). Tension, contraction and tissue morphogenesis. Development *144*, 4249–4260.
7. Sun, Z., Amourda, C., Shagirov, M., Hara, Y., Saunders, T.E., and Toyama, Y. (2017). Basolateral protrusion and apical contraction cooperatively drive *Drosophila* germ-band extension. Nat. Cell Biol. 2017 194 *19*, 375–383.
8. Higashi, T., and Miller, A.L. (2017). Tricellular junctions: How to build junctions at the TRICkiest points of epithelial cells. Mol. Biol. Cell *28*, 2023–2034.
9. Bosveld, F., and Bellaïche, Y. (2020). Tricellular junctions. Curr. Biol. *30*, R249–R251.
10. Uechi, H., and Kuranaga, E. (2019). The Tricellular Junction Protein Sidekick Regulates Vertex Dynamics to Promote Bicellular Junction Extension. Dev. Cell *50*, 327-338.e5.
11. Letizia, A., He, D., Astigarraga, S., Colombelli, J., Hatini, V., Llimargas, M., and Treisman, J.E. (2019). Sidekick Is a Key Component of Tricellular Adherens Junctions that Acts to Resolve Cell Rearrangements. Dev. Cell *50*, 313-326 e5.
12. Finegan, T.M., Hervieux, N., Nestor-Bergmann, A., Fletcher, A.G., Blanchard, G.B., and Sanson, B. (2019). The tricellular vertex-specific adhesion molecule Sidekick facilitates polarised cell intercalation during *Drosophila* axis extension. PLOS Biol. *17*, e3000522.
13. Vanderleest, T.E., Smits, C.M., Xie, Y., Jewett, C.E., Blankenship, J.T., and Loerke, D. (2018). Vertex sliding drives intercalation by radial coupling of adhesion and actomyosin networks during *Drosophila* germband extension. eLife *7*, e34586.
14. Razzell, W., Bustillo, M.E., and Zallen, J.A. (2018). The force-sensitive protein Ajuba regulates cell adhesion during epithelial morphogenesis. J. Cell Biol. *217*, 3715–3730.
15. Yu, H.H., and Zallen, J.A. (2020). Abl and Canoe/Afadin mediate mechanotransduction at tricellular junctions. Science *370*, eaba5528.
16. Ikawa, K., and Sugimura, K. (2018). AIP1 and cofilin ensure a resistance to tissue tension and promote directional cell rearrangement. Nat. Commun. *9*, 3295.

618 17. Pannekoek, W.J., de Rooij, J., and Gloerich, M. (2019). Force transduction by
619 cadherin adhesions in morphogenesis. F1000Research *8*, 1044.

620 18. Clarke, D.N., and Martin, A.C. (2021). Actin-based force generation and cell
621 adhesion in tissue morphogenesis. Curr. Biol. *31*, R667–R680.

622 19. Charras, G., and Yap, A.S. (2018). Tensile Forces and Mechanotransduction at
623 Cell–Cell Junctions. Curr. Biol. *28*, R445–R457.

624 20. Rauskolb, C., Cervantes, E., Madere, F., and Irvine, K.D. (2019). Organization
625 and function of tension-dependent complexes at adherens junctions. J. Cell Sci.
626 *132*, jcs224063.

627 21. Sawyer, J.K., Choi, W., Jung, K.C., He, L., Harris, N.J., and Peifer, M. (2011).
628 A contractile actomyosin network linked to adherens junctions by Canoe/afadin
629 helps drive convergent extension. Mol. Biol. Cell *22*, 2491–2508.

630 22. Lee, T., and Luo, L. (1999). Mosaic Analysis with a Repressible Cell Marker for
631 Studies of Gene Function in Neuronal Morphogenesis. Neuron *22*, 451–461.

632 23. Dunn, B.S., Rush, L., Lu, J.Y., and Xu, T. (2018). Mutations in the *Drosophila*
633 tricellular junction protein M6 synergize with Ras^{V12} to induce apical cell
634 delamination and invasion. Proc. Natl. Acad. Sci. *115*, 8358–8363.

635 24. Wittek, A., Hollmann, M., Schleutker, R., and Luschnig, S. (2020). The
636 Transmembrane Proteins M6 and Anakonda Cooperate to Initiate Tricellular
637 Junction Assembly in Epithelia of *Drosophila*. Curr. Biol. *30*, 4254–4262.

638 25. Ito, Y., Honda, A., and Igarashi, M. (2018). Glycoprotein M6a as a signaling
639 transducer in neuronal lipid rafts. Neurosci. Res. *128*, 19–24.

640 26. Esmangart de Bournonville, T., and Le Borgne, R. (2020). Interplay between
641 Anakonda, Gliotactin, and M6 for Tricellular Junction Assembly and Anchoring
642 of Septate Junctions in *Drosophila* Epithelium. Curr. Biol. *30*, 4245-4253.

643 27. de Gennes, P.-G., Brochard-Wyart, F., and Quéré, D. (2004). Capillarity and
644 Wetting Phenomena. Capillarity Wetting Phenom.

645 28. Prost, J., Jülicher, F., and Joanny, J.F. (2015). Active gel physics. Nat. Phys. *11*,
646 111–117.

647 29. Bardet, P.L., Guirao, B., Paoletti, C., Serman, F., Léopold, V., Bosveld, F., Goya,
648 Yû., Mirouse, V., Graner, F., and Bellaïche, Y. (2013). PTEN Controls Junction
649 Lengthening and Stability during Cell Rearrangement in Epithelial Tissue. Dev.
650 Cell *25*, 534–546.

651 30. Alfonso, J., Fernández, M.E., Cooper, B., Flugge, G., and Frasch, A.C. (2005).
652 The stress-regulated protein M6a is a key modulator for neurite outgrowth and
653 filopodium/spine formation. Proc. Natl. Acad. Sci. *102*, 17196–17201.

654 31. Jodoin, J.N., Coravos, J.S., Chanet, S., Vasquez, C.G., Tworoger, M., Kingston,
655 E.R., Perkins, L.A., Perrimon, N., and Martin, A.C. (2015). Stable Force Balance
656 between Epithelial Cells Arises from F-Actin Turnover. Dev. Cell *35*, 685–697.

657 32. Wang, Y.C., Khan, Z., Kaschube, M., and Wieschaus, E.F. (2012). Differential
658 positioning of adherens junctions is associated with initiation of epithelial
659 folding. Nature *484*, 390–393.

660 33. Nestor-Bergmann, A., Blanchard, G.B., Hervieux, N., Fletcher, A.G., Étienne,
661 J., and Sanson, B. (2022). Adhesion-regulated junction slippage controls cell
662 intercalation dynamics in an Apposed-Cortex Adhesion Model. PLOS Comput.
663 Biol. *18*, e1009812.

34. Bosveld, F., Markova, O., Guirao, B., Martin, C., Wang, Z., Pierre, A., Balakireva, M., Gaugue, I., Ainslie, A., Christophorou, N., et al. (2016). Epithelial tricellular junctions act as interphase cell shape sensors to orient mitosis. Nature *530*, 495–498.

35. López-Gay, J. M., Nunley, H., Spencer, M., di Pietro, F., Guirao, B., Bosveld, F., Markova, O., Gaugue, I., Pelletier, S., Lubensky, D.K., et al. (2020). Apical stress fibers enable a scaling between cell mechanical response and area in epithelial tissue. Science *370*, eabb2169.

36. Huang, J., Zhou, W., Dong, W., Watson, A.M., and Hong, Y. (2009). Directed, efficient, and versatile modifications of the *Drosophila* genome by genomic engineering. Proc. Natl. Acad. Sci. *106*, 8284–8289.

37. Pinheiro, D., Hannezo, E., Herszterg, S., Bosveld, F., Gaugue, I., Balakireva, M., Wang, Z., Cristo, I., Rigaud, S.U., Markova, O., et al. (2017). Transmission of cytokinesis forces via E-cadherin dilution and actomyosin flows. Nature *545*, 103–107.

38. Royou, A., Field, C., Sisson, J.C., Sullivan, W., and Karess, R. (2004). Reassessing the Role and Dynamics of Nonmuscle Myosin II during Furrow Formation in Early *Drosophila* Embryos. Mol. Biol. Cell *15*, 838–850.

39. Buszczak, M., Paterno, S., Lighthouse, D., Bachman, J., Planck, J., Owen, S., Skora, A.D., Nystul, T.G., Ohlstein, B., Allen, A., et al. (2007). The Carnegie Protein Trap Library: A Versatile Tool for *Drosophila* Developmental Studies. Genetics *175*, 1505–1531.

40. Lye, C.M., Naylor, H.W., Béné, B., and Sanson, B. (2014). Subcellular localisations of the CPTI collection of YFP-tagged proteins in *Drosophila* embryos. Development *141*, 4006–4017.

41. Sabino, D., Brown, N.H., and Basto, R. (2011). *Drosophila* Ajuba is not an Aurora-A activator but is required to maintain Aurora-A at the centrosome. J. Cell Sci. *124*, 1156–1166.

42. Morin, X., Daneman, R., Zavortink, M., and China, W. (2001). A protein trap strategy to detect GFP-tagged proteins expressed from their endogenous loci in *Drosophila*. Proc. Natl. Acad. Sci. *98*, 15050-15055.

43. Oda, H., and Tsukita, S. (2001). Real-time imaging of cell-cell adherens junctions reveals that *Drosophila* mesoderm invagination begins with two phases of apical constriction of cells. J. Cell Sci. *114*, 493–501.

44. Oda, H., Uemura, T., Shiomi, K., Nagafuchi, A., Tsukita, S., and Takeichi, M. (1993). Identification of a *Drosophila* homologue of alpha-catenin and its association with the armadillo protein. J. Cell Biol. *121*, 1133–1140.

45. Ishihara, S., and Sugimura, K. (2012). Bayesian inference of force dynamics during morphogenesis. J. Theor. Biol. *313*, 201–211.

46. Byri, S., Misra, T., Syed, Z.A., Bätz, T., Shah, J., Boril, L., Glashauser, J., Aegerter-Wilmsen, T., Matzat, T., Moussian, B., et al. (2015). The Triple-Repeat Protein Anakonda Controls Epithelial Tricellular Junction Formation in *Drosophila*. Dev. Cell *33*, 535–548.

47. Ito, K., Awano, W., Suzuki, K., Hiromi, Y., and Yamamoto, D. (1997). The *Drosophila* mushroom body is a quadruple structure of clonal units each of which contains a virtually identical set of neurones and glial cells. Development *124*, 761–771.

48. Sugimura, K., and Ishihara, S. (2013). The mechanical anisotropy in a tissue promotes ordering in hexagonal cell packing. Development *140*, 4091–4101.

49. Guirao, B., Rigaud, S.U., Bosveld, F., Bailles, A., López-Gay, J., Ishihara, S., Sugimura, K., Graner, F., and Bellaïche, Y. (2015). Unified quantitative characterization of epithelial tissue development. eLife *4*, e08519.

50. Kanda, Y. (2012). Investigation of the freely available easy-to-use software 'EZR' for medical statistics. Bone Marrow Transplant. *48*, 452–458.

51. Huang, D.L., Bax, N.A., Buckley, C.D., Weis, W.I., and Dunn, A.R. (2017). Vinculin forms a directionally asymmetric catch bond with F-actin. Science *357*, 6352, 703–706.

52. Aigouy, B., Farhadifar, L., Staple, D. B., Sagner, A., Röper, J.-C., Jülicher, F., and Eaton, S. (2010). Cell Flow Reorients the Axis of Planar Polarity in the Wing Epithelium of *Drosophila*. Cell *142*, 773–786.

726 ## Figure legends
727
728 **Fig. 1 myo-II is transiently detached from the AJ during the junction exchange.**
729 (a) Schematics of the cellular structure analyzed in this study. An orange circle in the
730 left panel indicates the region shown in the right panel. Gray and red lines indicate the
731 plasma membrane and cortical myo-II.
732 (b) Image of myo-II-GFP in a null mutant background of *spaghetti-squash* (*sqh*), which
733 encodes a *Drosophila* gene of myosin regulatory light chain. Blue arrowhead points to
734 the rsMC.
735 (c) Time-lapse images of myo-II-mKate2 (red in upper panels, gray in middle panels)
736 and DE-cad-GFP (green in upper panels, gray in bottom panels) during cell
737 rearrangement in the *Drosophila* pupal wing. Blue, yellow, and magenta arrowheads
738 indicate the detachment of myo-II from the AJ, the separation of the myo-II signals,
739 and the formation of the PD junction, respectively. A green arrowhead points to the
740 DE-cad signal inside the rsMC.
741 (d, e) Quantification of the myo-II-mKate2 signal intensity based on time-lapse data
742 captured at 25–26.5 h APF at 25 °C. (d) The myo-II-mKate2 signal intensity along the
743 vertical (AP) or horizontal (PD) edges (v_1, v_2, h_1, and h_2 in a schematic shown in the
744 top) of rsMC at the time point when the rsMC was formed. (e) The myo-II-mKate2
745 signal intensity around the rsMC is measured along the line ROI, which aligns along
746 the horizontal (PD) axis. Line colors represent the timing of measurement as shown in
747 the upper left corner, where the red line corresponds to the time of rsMC formation.
748 (f) Images of mCD8-GFP (gray in left panels, green in right panels) and myo-II-mKate2
749 (gray in middle panels, red in right panels) at 24 h APF. Arrowheads point to the mCD8-
750 GFP signal inside the rsMC.
751 (g, h) Images of an AJ marker, DE-cad-mTagRFP (gray in left panels, red in right
752 panels) and myo-II-GFP (gray in middle panels, green in right panels) at 24 h APF. The
753 vertical section along the dashed line in (g) is shown in (h).
754 (i–k) Images of an SJ marker, Dlg-GFP (gray in left panels, green in right panels) and
755 myo-II-mKate2 (gray in middle panels, red in right panels) at 24 h APF. (i, j) Top-view
756 along the different z-planes indicated at the bottom. (k) Side-view along the dashed line
757 in (i).
758 (l) Time-lapse images of Sdk-YFP (green in upper panels, gray in middle panels) and
759 myo-II-mKate2 (red in upper panels, gray in bottom panels) during cell rearrangement.
760 Arrowheads point to the Sdk-YFP signal at reconnecting TCJs.
761 Mann-Whitney *U* test: Vertical vs. Horizontal, $P < 0.001$ (d). The number of rsMCs (d)
762 and the number of ROIs (e) examined are indicated. Data are presented as the mean ±
763 s.d. (d, e). Scale bars: 2 μm (b, c, f–i, k, l).
764
765 **Fig. 2 The Jub-GFP signal is transiently weakened during the junction exchange.**

766 (a, b) Time-lapse images of myo-II-mKate2 (upper) and DE-cad-GFP (lower) with the
767 indicated genotypes (a, *jub* RNAi and b, *cno* RNAi). Blue and magenta arrowheads
768 point to the rsMC.
769 (c–e) Quantification of RNAi phenotypes. Junction length at the time point of rsMC
770 formation (c), the temporal average of rsMC area (d), and the fraction of rsMC time
771 duration (e) for each genotype based on time-lapse data captured at 25–26.5 h APF. In
772 (e), rsMC time duration is defined as the length of time between the formation and
773 fission of the rsMC.
774 (f) Images of mCD8-GFP (gray in left panel, green in right panel) and myo-II-mKate2
775 (gray in middle panel, red in right panel) at 24 h APF in *jub* RNAi cells. Arrowheads
776 point to the mCD8-GFP signal inside the rsMC.
777 (g) The correlation between the time average of rsMC area and the average area of four
778 cells surrounding the rsMC with the indicated genotypes (blue: *WT*, orange: *jub* RNAi,
779 green: *cno* RNAi, red; *Dα-cat* RNAi, purple: *vinc* RNAi and light blue: *m6* RNAi). The
780 correlation coefficient is 0.04.
781 (h) The myo-II-mkate2 signal intensity along the remodeling AP junctions at 3 min
782 before the rsMC formation for indicated genotypes.
783 (i) Time-lapse images of Jub-GFP (upper) and myo-II-mKate2 (lower). Blue and
784 magenta arrowheads indicate the decrease in Jub-GFP signal, and the formation of the
785 PD junction, respectively.
786 (j) Quantifications of Jub-GFP signal intensity around the rsMC based on time-lapse
787 data captured at 25–26 h APF in *WT* cells. The Jub-GFP signal intensity along the line
788 ROI at each position along the PD axis is plotted. Line colors represent the timing of
789 measurement as shown in the upper left corner, where purple line corresponds to the
790 time of rsMC formation.
791 Steel-Dwass test: *WT* vs. *jub* RNAi, $P < 0.001$, *WT* vs. *cno* RNAi, $P < 0.001$, *WT* vs.
792 *Dα-cat* RNAi, $P < 0.001$, *WT* vs. *vinc* RNAi, $P > 0.5$ (c), *WT* vs. *jub* RNAi, $P < 0.001$,
793 *WT* vs. *cno* RNAi, $P < 0.001$, *WT* vs. *Dα-cat* RNAi, $P < 0.001$, *WT* vs. *vinc* RNAi, $P >$
794 0.5 (d), *WT* vs. *jub* RNAi, $P > 0.5$, *WT* vs. *cno* RNAi, $P < 0.001$, *WT* vs. *Dα-cat* RNAi,
795 $P < 0.001$, *WT* vs. *vinc* RNAi, $P > 0.5$ (h). Student's *t*-test: the second time point vs. the
796 last time point, $P < 0.001$ (j); this result indicated that the drop of Jub-GFP signal
797 intensity at the time of rsMC formation was statistically significant. The number of
798 rsMCs (c–e, g) and the number of junctions examined (h, j) are indicated. Data are
799 presented as box plots (c, d) and as the mean ± s.d. (h, j). Scale bars: 2 μm (a, f, i).
800
801 **Fig. 3 Interplay between Jub and M6 during the junction exchange.**
802 (a) Magnified images of myo-II-GFP (gray in left panel, green in right panel) and DE-
803 cad-mTagRFP (gray in middle panel, red in right panel) at the tricellular junction (*i.e.*,
804 at the cell vertex). myo-II is occasionally detached from the vertex of non-remodeling
805 junctions and forms a rsMC-like structure (arrowheads).

806 (b) Time-lapse images of myo-II-mKate2 (upper) and DE-cad-GFP (lower) in *m6*
807 RNAi wing.
808 (c–e) Quantification of RNAi phenotypes. Junction length at the time point of rsMC
809 formation (c), the temporal average of rsMC area (d), and the fraction of rsMC time
810 duration (e) for each genotype based on time-lapse data captured at 25–26.5 h APF.
811 (f) Time-lapse images of Jub-GFP (upper) and myo-II-mKate2 (lower) in *m6* RNAi
812 wing. Arrowheads indicate the retention of Jub inside the rsMC.
813 (g) Quantifications of Jub-GFP signal intensity around the rsMC based on time-lapse
814 data captured at 25–26 h APF in *m6* RNAi cells (see the legend of Fig. 2j for details).
815 (h, i) Images of M6-GFP at 24 h APF in wings of the indicated genotypes (h, *WT* and
816 i, *aka* RNAi).
817 (j, k) Images of Aka-GFP at 24 h APF in wings of the indicated genotypes (j, *WT* and
818 k, *m6* RNAi).
819 (l–q) Images of M6-GFP (green) and DE-cad-mTagRFP (magenta) in *WT* (l–n) and *jub*
820 RNAi (o–q) wings. In left panels, images along the AJ planes (l, o) and more basal
821 planes (m, p) are shown as indicated at the bottom.
822 Steel-Dwass test: *WT* vs. *m6* RNAi, $P < 0.001$, *WT* vs. *aka* RNAi, $P < 0.001$, *WT* vs.
823 *sdk* RNAi, $P < 0.001$ (c), *WT* vs. *m6* RNAi, $P < 0.05$, *WT* vs. *aka* RNAi, $P > 0.05$, *WT*
824 vs. *sdk* RNAi, $P < 0.01$ (d). Welch's *t*-test: *WT* vs. *m6* RNAi, $P < 0.01$; this result
825 confirmed that the Jub-GFP signal intensity at the time point of rsMC formation was
826 statistically different among *WT* and *m6* RNAi cells. The number of rsMCs (c–e) and
827 the number of junctions examined (g) are indicated. Data are presented as box plots (c,
828 d) and the mean ± s.d. (g). Scale bars: 2 μm (a, b, f, h, j, m, n).
829
830 **Fig. 4 A mechanical model of the detachment/attachment of cortical myo-II.**
831 (a) Schematics of the attached and detached states of cortical myo-II cables in a single
832 cell. An orange circle in the left panel indicates the region shown in the middle and
833 right panels. In the attached state, myo-II cables, which are indicated by blue lines, run
834 along cell contact surfaces. In the detached state, myo-II cables are detached from cell
835 contact surfaces, as indicated by red lines. L_0: the length of vertical remodeling
836 junction; L_1: the length of junctions connecting to the remodeling junction; l: the length
837 of the connecting junctions, from which cortical myo-II is detached; θ: the half-angle
838 between connecting junctions.
839 (b) Schematics of the attached and detached states of cortical myo-II cables in four cell.
840 L_0': the length of horizontal newly generated junction; $\theta' + 90°$: the angle between the
841 connecting junction and the horizontal newly generated junction.
842 (c–e) Quantification of the geometrical parameters of the theoretical model of myo-II
843 cables. (c) Average length of the remodeling (L_0) and connection junctions (L_1) at the
844 time point of rsMC formation in *WT* cells. For measuring L_1, the average length of four
845 connecting junctions was calculated for each rsMC. (d) Frequency of the half-angle
846 between connecting junctions (θ) at the time point of rsMC formation. The average

half-angle value of the upper and bottom connecting junctions was calculated for each rsMC. (e) Quantification of junction angles (θ and θ') before, during, and after the rsMC formation (before: 9 min before the rsMC formation; during: the time point of the rsMC formation; after: 0–2 min after the rsMC fission).
(f) Plot of myo-II-mKate2 signal intensity along shrinking AP junctions prior to the myo-II detachment (n = 7). Bold line shows the average values. $t = 0$ indicates the time point when the myo-II gap was formed.
(g) Free energies for the attached and detached states, F_a and F_d. Difference of the free energies $F_d - F_a$ is shown as a function of l. The energy scale is in arbitrary unit. The parameters are set as $\gamma = 6.0$, $\sigma = 1.0, \theta = 60°$, and $L_0 = 0.4\ \mu m$.
(h) A phase diagram of the attached state and detached state on a γ/σ-l plane. Solid and dotted lines indicate $\gamma = \sigma(L_0 + 2l)/2(1 - \cos\theta)l$ above which the detached state is energetically preferable. $\gamma^* \equiv \sigma/(1 - \cos\theta)$ is the threshold tension for the detachment state to exist. $\theta = 60°$.
(i, j) Phase diagrams of the attached and detached states on the γ/σ–γ'/σ plane. Thick black lines indicate the conditions above which the detached state is preferable. The parameters are set as (i) $\theta = 60°, L_0 = 0.4$, and $l = 0.2$, and (j) $\theta' = 50°, L_0' = 0.4$, and $l = 0.2$. In (j), the same condition for $L_0' = 0.6$ is also shown as a dotted line.
Paired *t*-test: During vs. After, $P < 0.001$ (e). The number of rsMCs (c, d) and the number of junctions examined (e) are indicated. Data are presented as the mean ± s.d.

Fig. 5 Cortical myo-II did not reattach to the AJ in *pten* RNAi cells.
(a) Quantifications of myo-II-mKate2 signal intensity around the rsMC based on time-lapse data captured at 25–26.5 h APF at 25 °C in *pten* RNAi cells. The myo-II-mKate2 signal intensity along the line ROI, which aligns along the horizontal (PD) axis, is plotted. Line colors represent the timing of measurement as shown in the upper left corner, where the red line corresponds to the time of rsMC formation.
(b) Time-lapse images of myo-II-mKate2 (upper) and DE-cad-GFP (lower) in *pten* RNAi wing. Blue and magenta arrowheads point to the rsMC.
(c–e) Quantification of RNAi phenotypes. Junction length at the time point of rsMC formation (c), the temporal average of rsMC area (d), and the fraction of rsMC time duration (e) for each genotype based on time-lapse data captured at 25–26.5 h APF.
Steel-Dwass test: *WT* vs. *pten* RNAi, $P < 0.001$ (c), *WT* vs. *pten* RNAi, $P > 0.5$ (d).The number of ROIs (a) and the number of rsMCs examined (c–e) are indicated. Data are presented as the mean ± s.d. (a) and box plots (c, d). Scale bar: 2 μm (b).

Fig. 6 Summary of the mechanism of junction exchange.
(a) A schematic illustrating molecular interactions and the junction geometry during three phases in cell rearrangement. The concentrations of myo-II and Jub are depicted by color intensity (myo-II: light orange to red, Jub: light green to green). L_0: the length of vertical remodeling junction; ΔF: an energy barrier for the detachment of cortical

myo-II ($= \sigma L_0$); γ_{min}: the value of tension of myo-II cables to separate the detached and attached regions ($= \sigma(L_0 + 2l)/2(1 - \cos\theta)l$).
(b–d) Schematic illustrating molecular interactions and the junction geometry in the indicated genotypes (b, *jub* RNAi; c, *m6* RNAi and d, *pten* RNAi). See the main text for details.

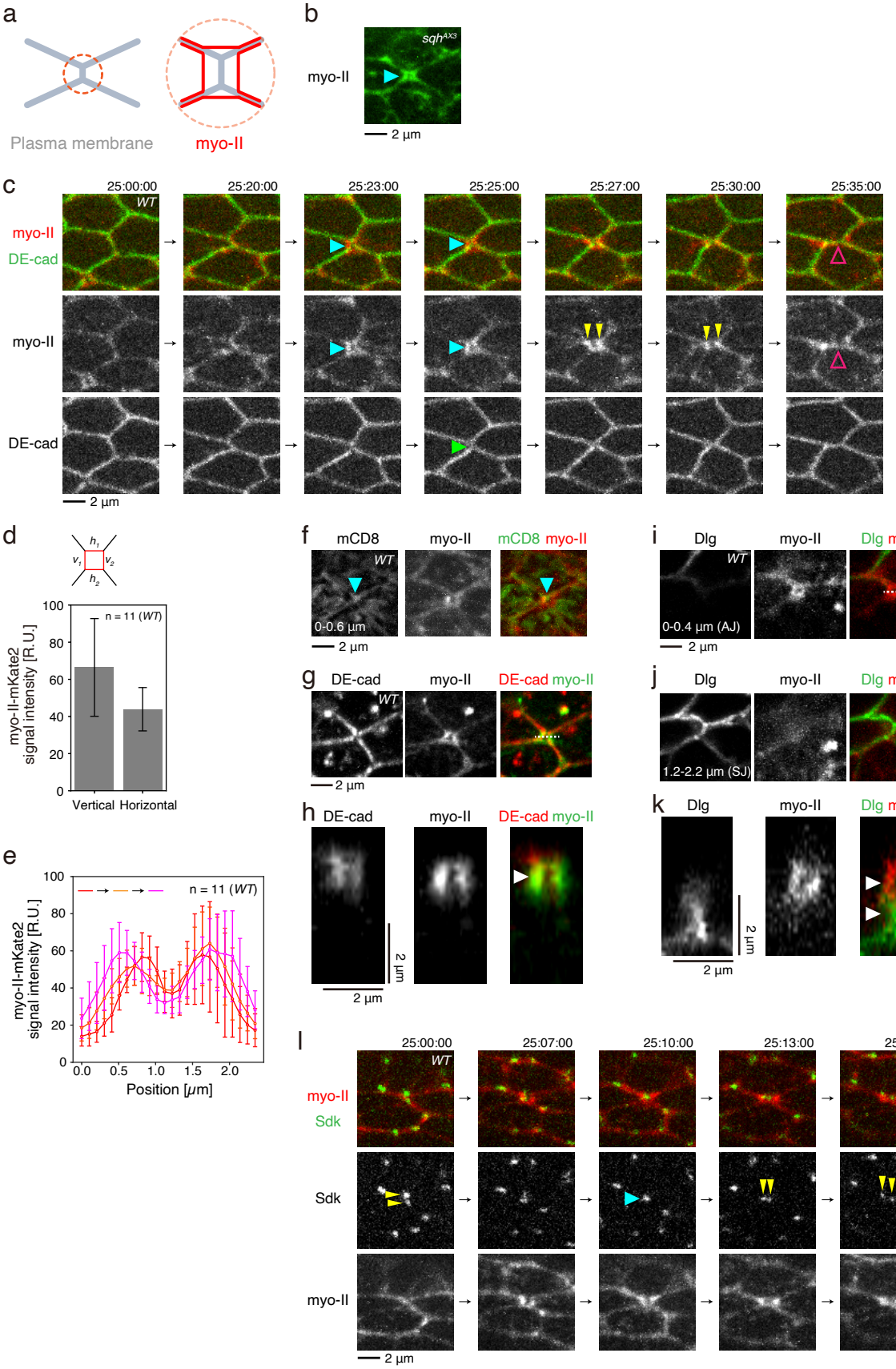
a
Plasma membrane
myo-II
b
myo-II
sqh^AX3
2 µm
c
25:00:00
25:20:00
25:23:00
25:25:00
25:27:00
25:30:00
25:35:00
WT
myo-II
DE-cad
myo-II
DE-cad
2 µm
d
h1
v1
v2
h2
n = 11 (WT)
myo-II-mKate2 signal intensity [R.U.]
Vertical
Horizontal
e
n = 11 (WT)
myo-II-mKate2 signal intensity [R.U.]
Position [µm]
f
mCD8
myo-II
mCD8 myo-II
WT
0-0.6 µm
2 µm
g
DE-cad
myo-II
DE-cad myo-II
WT
2 µm
h
DE-cad
myo-II
DE-cad myo-II
2 µm
2 µm
i
Dlg
myo-II
Dlg myo-II
WT
0-0.4 µm (AJ)
2 µm
j
Dlg
myo-II
Dlg myo-II
1.2-2.2 µm (SJ)
k
Dlg
myo-II
Dlg myo-II
2 µm
2 µm
l
25:00:00
25:07:00
25:10:00
25:13:00
25:15:00
WT
myo-II
Sdk
Sdk
myo-II
2 µm

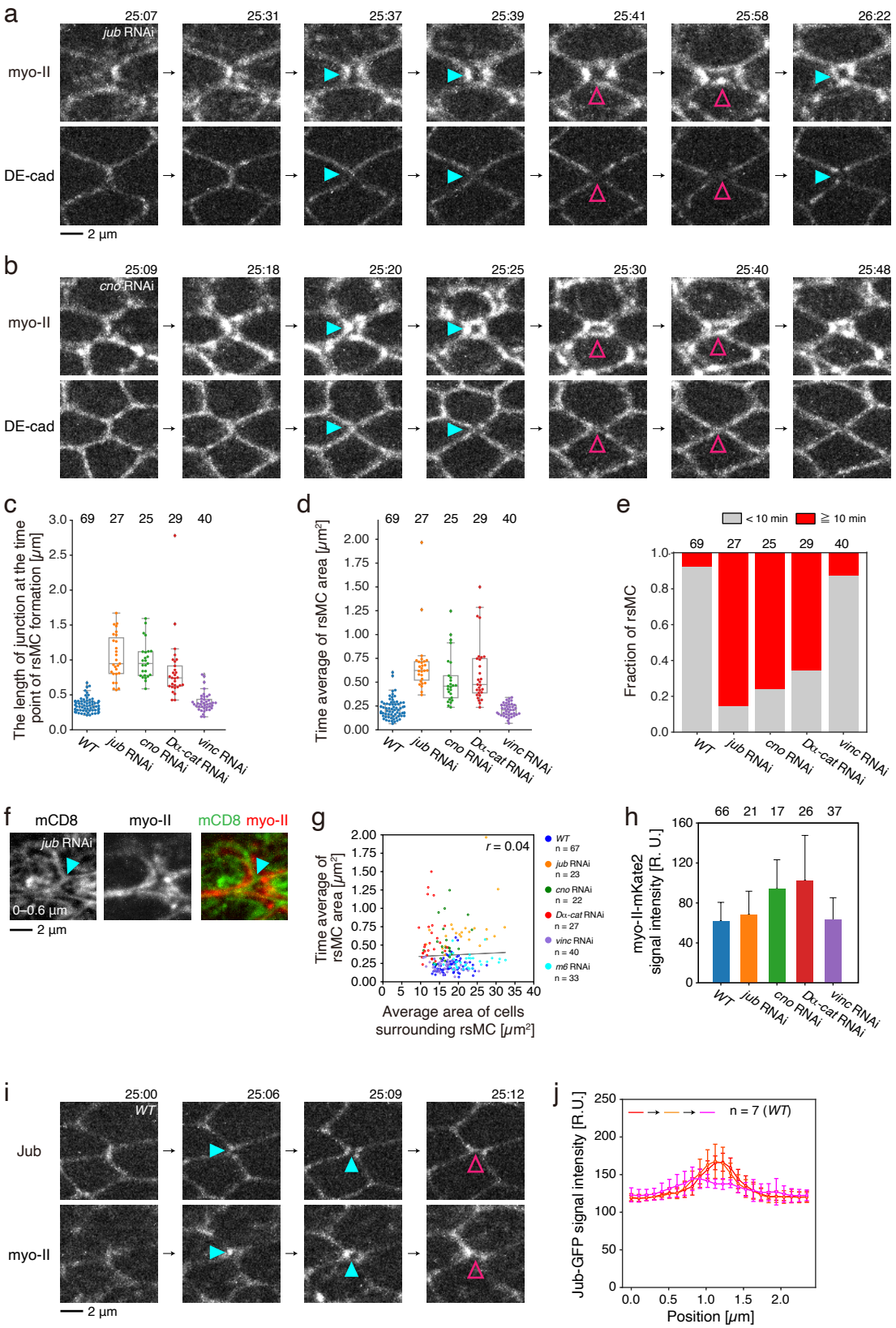
a
25:07
25:31
25:37
25:39
25:41
25:58
26:22
jub RNAi
myo-II
DE-cad
2 μm
b
25:09
25:18
25:20
25:25
25:30
25:40
25:48
cno RNAi
myo-II
DE-cad
c
The length of junction at the time point of rsMC formation [μm]
69 27 25 29 40
WT
jub RNAi
cno RNAi
Dα-cat RNAi
vinc RNAi
d
Time average of rsMC area [μm²]
69 27 25 29 40
WT
jub RNAi
cno RNAi
Dα-cat RNAi
vinc RNAi
e
< 10 min
≧ 10 min
Fraction of rsMC
69 27 25 29 40
WT
jub RNAi
cno RNAi
Dα-cat RNAi
vinc RNAi
f
mCD8
myo-II
mCD8 myo-II
jub RNAi
0–0.6 μm
2 μm
g
Time average of rsMC area [μm²]
r = 0.04
Average area of cells surrounding rsMC [μm²]
WT n = 67
jub RNAi n = 23
cno RNAi n = 22
Dα-cat RNAi n = 27
vinc RNAi n = 40
m6 RNAi n = 33
h
myo-II-mKate2 signal intensity [R. U.]
66 21 17 26 37
WT
jub RNAi
cno RNAi
Dα-cat RNAi
vinc RNAi
i
25:00
25:06
25:09
25:12
WT
Jub
myo-II
2 μm
j
Jub-GFP signal intensity [R.U.]
n = 7 (WT)
Position [μm]

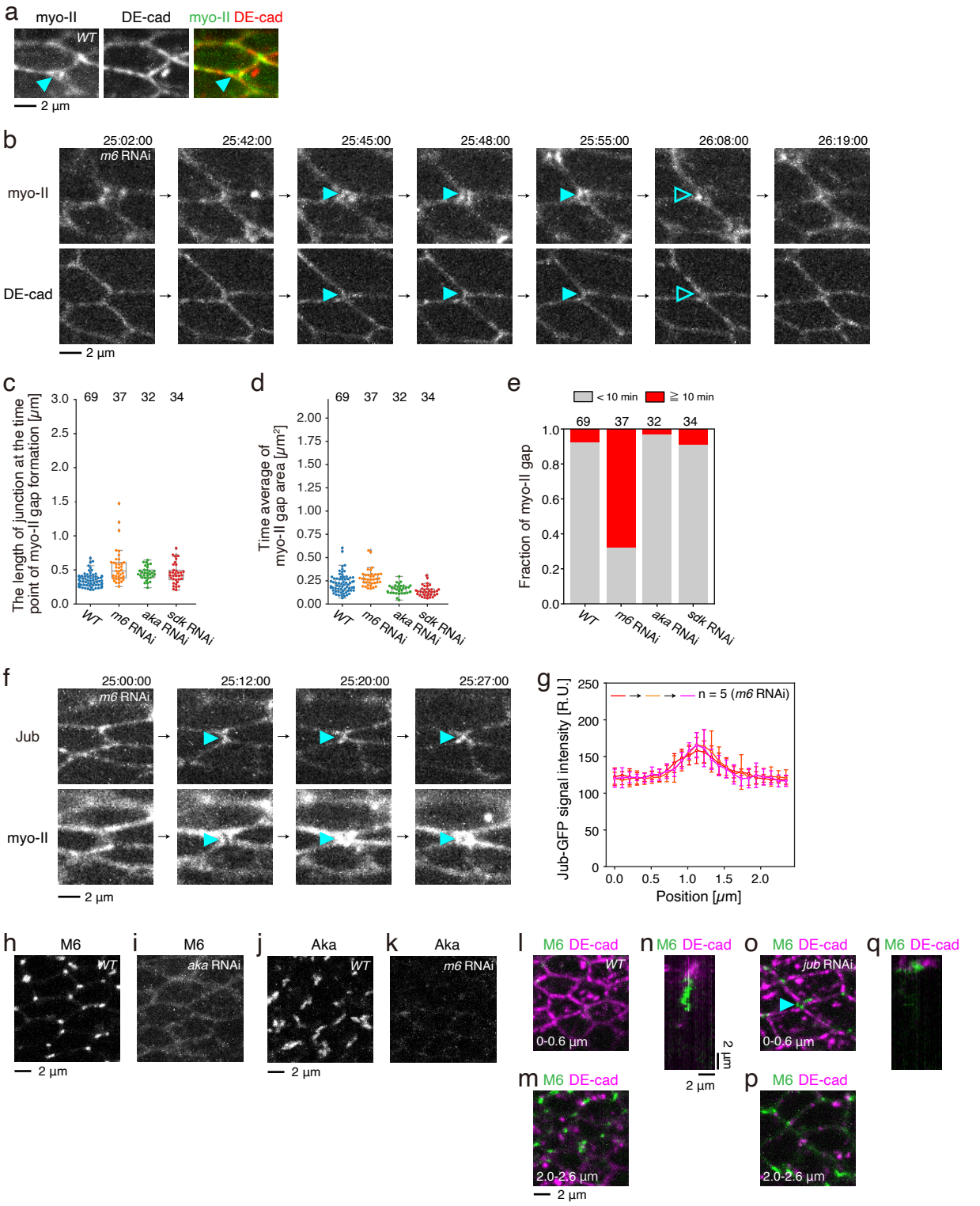
a
myo-II
DE-cad
myo-II DE-cad
WT
2 μm
b
25:02:00
25:42:00
25:45:00
25:48:00
25:55:00
26:08:00
26:19:00
m6 RNAi
myo-II
DE-cad
2 μm
c
The length of junction at the time point of myo-II gap formation [μm]
69 37 32 34
WT
m6 RNAi
aka RNAi
sdk RNAi
d
Time average of myo-II gap area [μm²]
69 37 32 34
WT
m6 RNAi
aka RNAi
sdk RNAi
e
< 10 min
≧ 10 min
Fraction of myo-II gap
69 37 32 34
WT
m6 RNAi
aka RNAi
sdk RNAi
f
25:00:00
25:12:00
25:20:00
25:27:00
m6 RNAi
Jub
myo-II
2 μm
g
n = 5 (m6 RNAi)
Jub-GFP signal intensity [R.U.]
Position [μm]
h
M6
WT
2 μm
i
M6
aka RNAi
j
Aka
WT
2 μm
k
Aka
m6 RNAi
l
M6 DE-cad
WT
0-0.6 μm
n
M6 DE-cad
2 μm
2 μm
o
M6 DE-cad
jub RNAi
0-0.6 μm
q
M6 DE-cad
m
M6 DE-cad
2.0-2.6 μm
2 μm
p
M6 DE-cad
2.0-2.6 μm

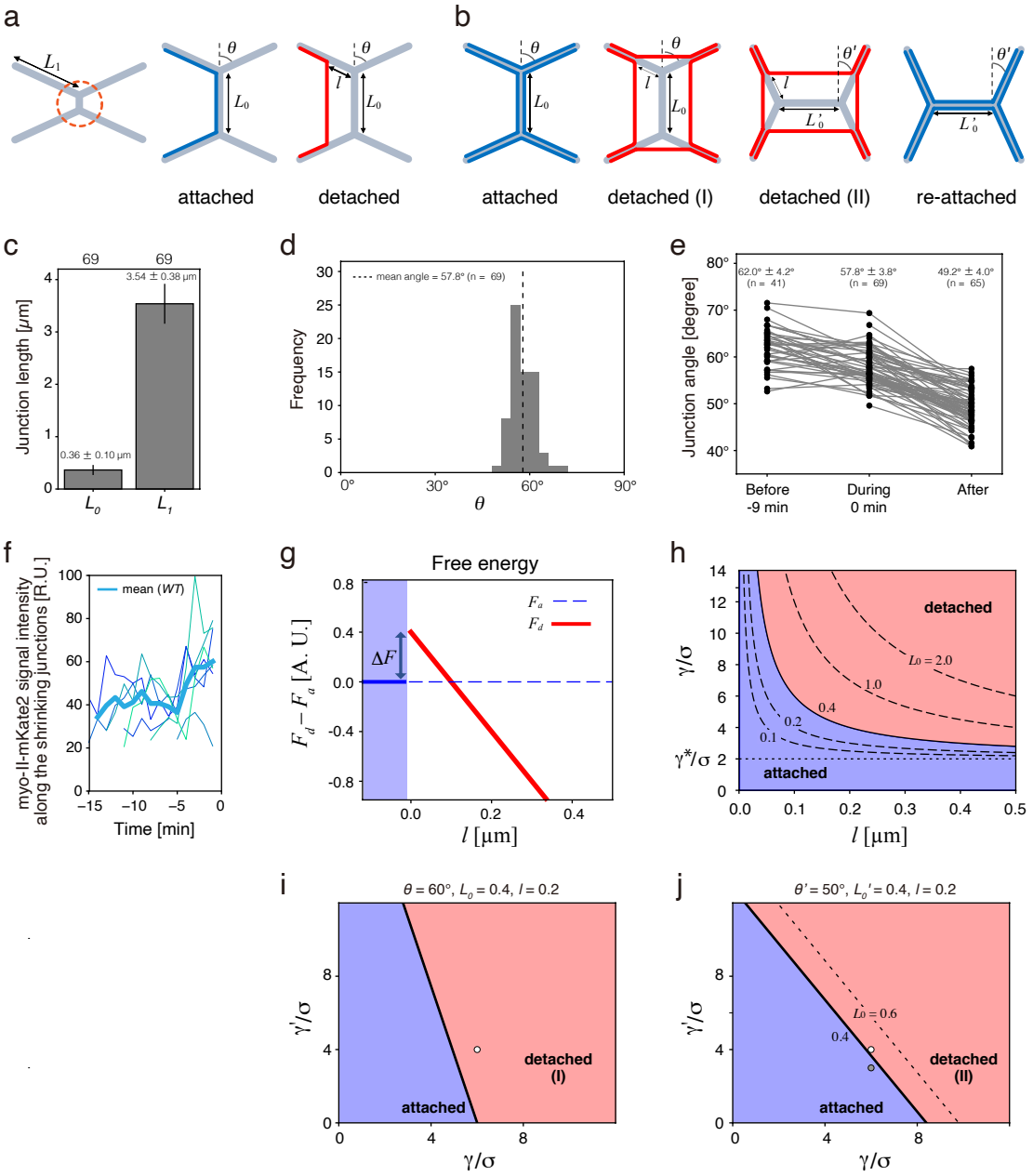
a
b
attached
detached
attached
detached (I)
detached (II)
re-attached
c
69
69
3.54 ± 0.38 µm
0.36 ± 0.10 µm
Junction length [µm]
d
mean angle = 57.8° (n = 69)
Frequency
e
62.0° ± 4.2° (n = 41)
57.8° ± 3.8° (n = 69)
49.2° ± 4.0° (n = 65)
Junction angle [degree]
Before -9 min
During 0 min
After
f
mean (WT)
myo-II-mKate2 signal intensity along the shrinking junctions [R.U.]
Time [min]
g
Free energy
ΔF
l [µm]
h
detached
attached
γ/σ
γ*/σ
l [µm]
i
θ = 60°, L0 = 0.4, l = 0.2
detached (I)
attached
γ'/σ
γ/σ
j
θ' = 50°, L0' = 0.4, l = 0.2
detached (II)
attached
γ'/σ
γ/σ

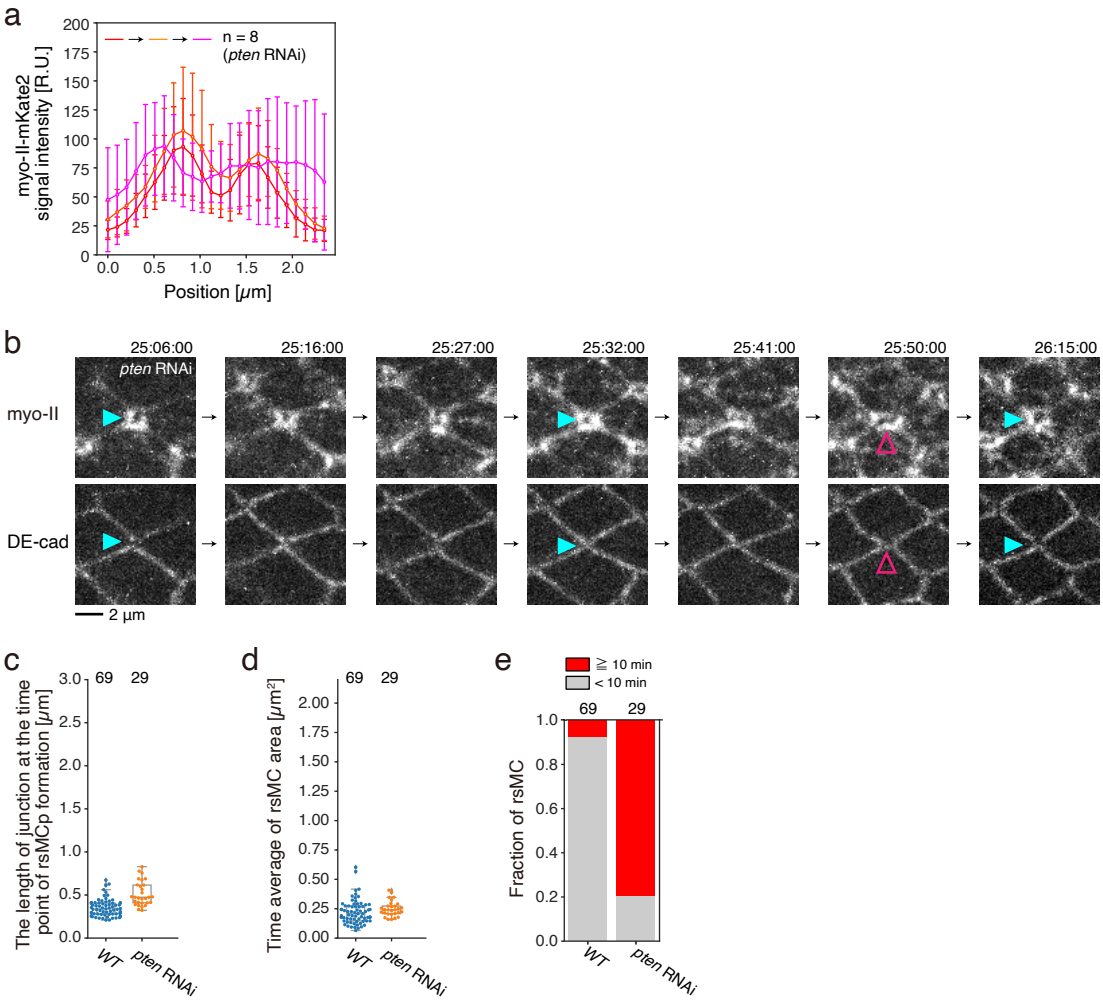
a
n = 8
(pten RNAi)
myo-II-mKate2 signal intensity [R.U.]
Position [μm]
b
25:06:00
25:16:00
25:27:00
25:32:00
25:41:00
25:50:00
26:15:00
pten RNAi
myo-II
DE-cad
2 μm
c
The length of junction at the time point of rsMCp formation [μm]
69
29
WT
pten RNAi
d
Time average of rsMC area [μm²]
69
29
WT
pten RNAi
e
≧ 10 min
< 10 min
Fraction of rsMC
69
29
WT
pten RNAi

a

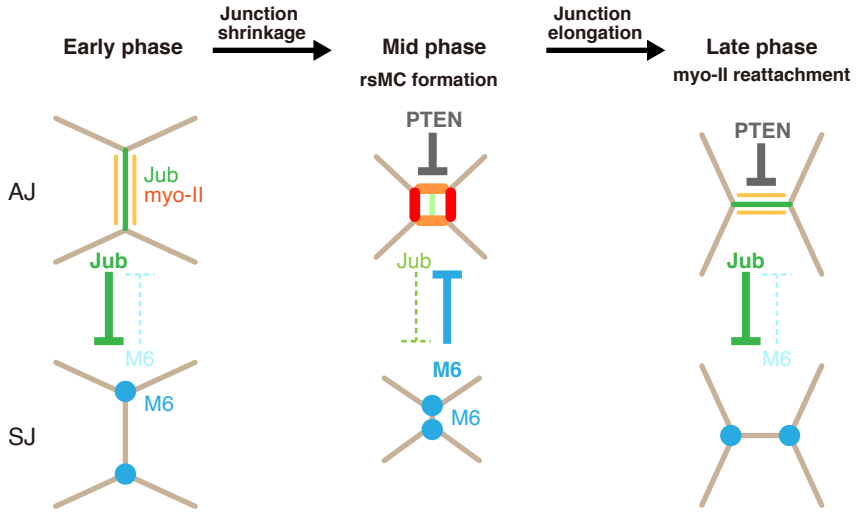

L_0	Long	Short	Long
ΔF, γ_{min}	Large	Small	Large

b

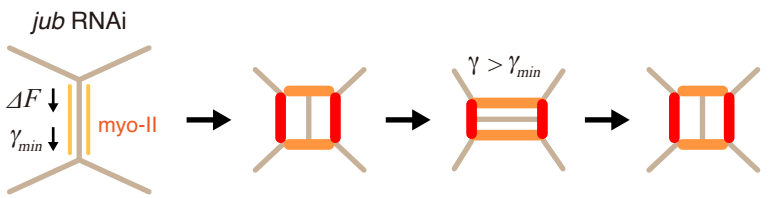

c

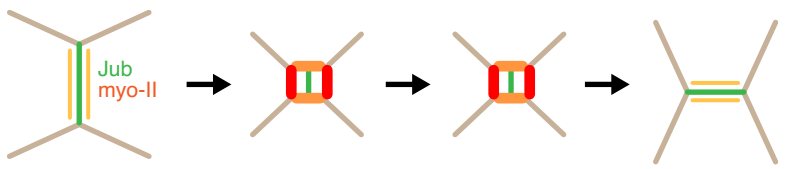
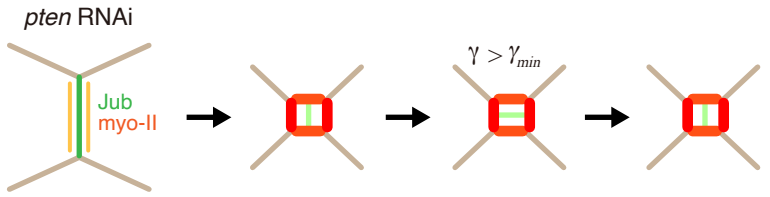
d